# MASTERARBEIT

Titel der Masterarbeit

# Formation of Calcite and Siderite Concretions from Eastern Austria

verfasst von

## Lydia Baumann BSc

angestrebter akademischer Grad

## Master of Science (MSc)

Wien, 2015

Hereby, I confirm to have composed this master's thesis independently, without the aid of any, than the sources declared as such. I have explicitly cited all material, which has been used, either literally or by content. Further, this work has not been submitted or accepted for the award of any other degree or diploma in any university or institution, neither in Austria, nor abroad.

Lydia Baumann                                    Vienna, May 2015

# Table of contents

# Kurzfassung

Karbonatkonkretionen mit zwei unterschiedlichen geologischen Hintergründen wurden im Hinblick auf ihre Petrografie, stabile Kohlenstoff- und Sauerstoffisotope und Lipidbiomarkerinhalt untersucht. Karbonatkonkretionen sind im Wesentlichen Produkte des mikrobiellen Abbaus von organischem Material, wie zum Beispiel durch eisenreduzierende Bakterien, sulfatreduzierende Bakterien und methanogene Archaeen. Für diese Prokaryoten sind bestimmte Lipidbiomarker wie Hopanoide, endverzweigte Fettsäuren (Bakterien) und Isoprenoide (Archaeen) charakteristisch. Zwei verschiedene Typen von Konkretionen wurden untersucht: i) obermiozäne, septarische Kalzitkonkretionen des südlichen Wiener Beckens, eingebettet in brackische Sedimente, die von teilweise bituminösen, kalkigen Sanden, Schluffen und Tonen repräsentiert werden; ii) paläozäne-eozäne Sideritkonkretionen, eingeschlossen in marinen, sandigen bis schluffigen Turbiditen mit veränderlichen Karbonatanteilen und Mergellagen von der Oberen Gosausubgruppe in der nördlichen Steiermark. Die Kalzitkonkretionen bestehen zu einem Großteil aus kalzitischem Mikrosparit (80 bis 90 vol.%), sowie detritären Mineralen und Eisenoxidhydroxiden. Die septarischen Brüche zeigen zu unterschiedlichen Graden beginnende Zementierung mit Hundezahnkalzit. Framboidaler Pyrit tritt in einigen der Kalzitkonkretionen auf, was auf bakterielle Sulfatreduktion hindeutet. Die Sideritkonkretionen bestehen aus sogar noch feineren Karbonatkristallen, hauptsächlich Siderit (40 bis 70 vol.%), aber auch reichlich eisenhaltigem Kalzit, begleitet von Eisenoxidhydroxiden und detritären Mineralen. Die $\delta^{13}$C-Werte der Kalzitkonkretionen (−6.8 bis −4.2‰) spiegeln höchstwahrscheinlich eine Mischung von Karbonat aus bakterieller Oxidation von organischer Substanz mit marinem, bioklastischem Karbonat wieder. Die $\delta^{18}$O-Werte reichen von −8.8 bis −7.9‰, was in Übereinstimmung mit der Bildung in einer meteorischen Umgebung ist. Das umgebende Wirtssediment zeigt um etwa 1 bis 2‰ höhere $^{13}$C- und $^{18}$O-Werte. Die $^{13}$C-Werte des Siderits (−11.1 bis −7.5‰) weisen auf mikrobielle Veratmung von organischem Kohlenstoff hin und die $\delta^{18}$O-Werte (−3.5 bis +2.2‰) sind im Einklang mit einem marinen Sedimentationsraum. Im Gegensatz zu den Kalzitkonkretionen unterscheidet sich die stabile Kohlenstoffisotopie des Umgebungssediments wesentlich von den Sideritkonkretionen. Die $\delta^{13}$C-Werte des Gosausediments spiegeln marine Bedingungen wieder, während die Sauerstoffisotope am besten mit einer meteorischen Überprägung erklärt werden können. Die Lipidbiomarker wurden vor und nach der Auflösung des Karbonats der Konkretionen extrahiert, um ihre Authentizität zu garantieren und um rezente Oberflächenkontamination auszuschließen. Im Folgenden werden nur die Biomarker, die nach der Karbonatlösung extrahiert wurden, diskutiert, da von ihnen angenommen wird, dass sie mit der Konkretionsbildung in Verbindung stehen. Die Kalzitkonkretionen umfassen von Pflanzenwachsen stammende, langkettige *n*-Alkane, die signifikanten Eintrag von terrestrischen Blattwachsen repräsentieren. Bakterielle Komponenten, wie zum Beispiel endverzweigte Fettsäuren und Hopanoide wurden gefunden, allerdings in geringen Konzentrationen. Die Sideritkonkretionen enthalten aufgrund ihrer hohen thermischen Reife keine aussagekräftigen Biomarker. In keiner der

Konkretionen wurden Biomarker von Archaeen gefunden. In Anbetracht des Vorkommens von framboidalem Pyrit, den moderat niedrigen $\delta^{13}$C-Werten und dem Biomarkerinventar, hat Sulfatreduktion wohl tatsächlich zur Entstehung der Kalzitkonkretionen in einer Brackwasserumgebung beigetragen. Im Gegensatz dazu inhibieren fortwährende Sulfatreduktion und die daraus resultierende Produktion von Schwefelwasserstoff die Sideritfällung. Daher können die niedrigen $\delta^{13}$C-Werte der Sideritkonkretionen am besten durch bakterielle Eisenreduktion erklärt werden.

# Abstract

Carbonate concretions from two distinct settings have been studied for their petrography, stable carbon and oxygen isotopes, and lipid biomarker inventory. Generally, carbonate concretions are products of microbial degradation of organic matter, as for example by iron-reducing bacteria, sulfate-reducing bacteria and methanogenic archaea. Specific lipid biomarkers such as hopanoids, terminally-branched fatty acids (bacteria) and isoprenoids (archaea) are characteristic for these prokaryotes. Two different types of concretions were studied: i) Upper Miocene septarian calcite concretions of the southern Vienna Basin embedded in brackish sediments represented by partly bituminous calcareous sands, silts and clays; ii) Paleocene-Eocene siderite concretions enclosed in marine, sandy to silty turbidites with varying carbonate contents and marl layers from the Upper Gosau Subgroup in northern Styria. Calcite concretions consist of abundant calcite microspar (80 to 90 vol.%), as well as detrital minerals and iron oxyhydroxides. The septarian cracks display beginning cementation with dog-tooth calcite to varying degrees. Framboidal pyrite occurs in some of the calcite concretions, pointing to bacterial sulfate reduction. Siderite concretions consist of even finer carbonate crystals, mainly siderite (40 to 70 vol.%), but also abundant ferroan calcite, accompanied by iron oxyhydroxides and detrital minerals. The $\delta^{13}$C values of the calcite concretions (−6.8 to −4.2‰) most likely reflect a combination of bacterial organic matter oxidation and input of marine biodetrital carbonate. The $\delta^{18}$O values range from −8.8 to −7.9‰, agreeing with a formation within a meteoric environment. The surrounding host sediment shows slightly higher $^{13}$C and $^{18}$O values (1 to 2‰ higher). The siderite $\delta^{13}$C values (−11.1 to −7.5‰) point to microbial respiration of organic carbon and the $\delta^{18}$O values (−3.5 to +2.2‰) agree with a marine depositional environment. In contrast to the calcite concretions, the stable isotope composition of the host sediment differs significantly from the siderite concretions. The $\delta^{13}$C values of the Gosau host sediment reflect marine conditions, whereas the oxygen isotope values are best explained by secondary meteoric water overprint. Lipid biomarkers have been extracted before and after decalcification of the concretions in order to assess only pristine signatures and to exclude secondary surface contamination. In the following, only the biomarkers extracted after decalcification are discussed, since they are thought to reflect biomarkers when concretion formation took place. The calcite concretions comprise abundant plant wax derived long-chain *n*-alkanes,

reflecting high terrestrial input. Bacterial-derived, terminally-branched fatty acids and hopanoids were found, but with overall low contents. The siderite concretions did not yield indigenous biomarkers due to their high thermal maturity. No archaeal biomarkers were found in any of the concretions. Considering the presence of framboidal pyrite, the moderately low $\delta^{13}C$ values, and the biomarker inventory, bacterial sulfate reduction apparently contributed to the formation of the calcite concretions in a brackish environment. In contrast, ongoing sulfate reduction and resultant hydrogen sulfide production inhibit siderite precipitation. Therefore, the low $\delta^{13}C$ values of the siderite concretions are best explained by bacterial iron reduction.

# 1 Introduction

Concretions are confined bodies of clastic sediment lithified by authigenic minerals. They form during shallow burial of sediments, preferably within the first tens of meters when the surrounding sediment is still unconsolidated, and are, thus, products of early diagenesis (Blome & Albert, 1985; Pye et al., 1990; Duck, 1995; Mozley, 1996; Hounslow, 1997; Pratt, 2001; Raiswell & Fisher, 2004; Pearson et al., 2005; Pearson & Nelson, 2005). Sellés-Martínez (1996) provided an elaborate classification scheme of various concretionary bodies, distinguishing between cements, veins, nodules and concretions. Nodules and concretions are very similar. However, whereas concretions incorporate material of the host sediment, nodules contain solely authigenic phases. Concretions are usually spherical or ellipsoidal in shape, but also come as elongated, oblate, tubular, lobate or irregular bodies (Coleman et al., 1993; Coleman & Raiswell, 1995; Duck, 1995; Pratt, 2001, Lash & Blood, 2004; Pearson & Nelson, 2005; Loyd et al., 2012a; Thomka & Lewis, 2013). Concretion cements are composed of carbonate, phosphate, silica, sulfide, sulfate, and iron oxide minerals (Mozley, 1996; Sellés-Martínez, 1996; Pearson et al., 2005; Pearson & Nelson, 2005; Yli-Hemminki et al., 2014). Most common parageneses are carbonate concretions in clayey or sandy horizons, quartz or chert in limestones, and pyrite in black shales (Coleman, 1985; Sellés-Martínez, 1996), and the most common concretion-forming minerals are carbonates such as calcite, Mg-calcite, Fe-calcite, siderite and dolomite (Siegel et al., 1987; Pye et al., 1990; Coleman et al., 1993; Coleman & Raiswell, 1995; Mozley, 1996; Sellés-Martínez, 1996; Pearson et al., 2005; Pearson & Nelson, 2005; Loyd et al., 2012a). Concretion size varies from millimeters to meters, and estimated growth rates vary from tens to hundreds up to thousands of years for decimeter-sized concretions (Duck, 1995; Sellés-Martínez, 1996; Pratt, 2001; Lash & Blood, 2004; Loyd et al., 2012a; Thomka & Lewis, 2013). Concretions of meter size are assumed to take millions of years for their growth (Sellés-Martínez, 1996). In great contrast, Pye et al. (1990) described modern siderite concretions up to 40 cm in diameter, which were formed in few decades, because the host sediment, a salt marsh at the north Norfolk coast (UK), has only been deposited since World War II.

Many studies have developed detailed scenarios for the growth of concretions (Coleman & Raiswell, 1995; Mozley, 1996; Raiswell & Fisher, 2000; Loyd et al., 2014). Two opposing scenarios are favored, the "concentric growth" and the "pervasive growth" model. Raiswell & Fisher (2000) explain them very well in their paper: i) concentric growth: "…*the concentric growth model assumed that layers of tightly cemented carbonate were added successively to the outer surface of the concretion* […] *radius increases with time…*", and ii) pervasive growth: "…*where cement crystals grow simultaneously throughout the concretion volume (little or no radius increase with time…)*". During concentric growth, rigid, fully cemented layers are added until the final volume is reached only at the end of growth, whereas during pervasive growth the final

volume of the concretion is defined from the onset of cementation. The latter mode appears to produce only poorly lithified concretions (Raiswell & Fisher). However, a variety of complex intermediate growth modes may occur that fall between the two endmember modes. Most recent studies rather favor the pervasive growth scenario (e.g. Mozley, 1996; Raiswell & Fisher, 2000; Lash & Blood, 2004; Loyd et al. 2014).

The most common explanation of what is inducing the formation of the authigenic carbonate minerals of carbonate concretions is the microbial oxidation of buried organic matter under anaerobic conditions (Irwin et al., 1977; Siegel et al., 1987; Blome & Albert, 1985; Coleman, 1985; Pye et al., 1990; Coleman et al., 1993; Coleman & Raiswell, 1995; Sellés-Maínez, 1996; Mortimer & Coleman, 1997; Kiriakoulakis et al., 2000; Raiswell & Fisher, 2000; Lash & Blood, 2004; Raiswell & Fisher, 2004; Pearson et al., 2005; Pearson & Nelson, 2005; Reitner et al., 2005; Mortimer et al., 2011; Loyd et al., 2012a/b; Loyd et al., 2014). The biogeochemical processes that are believed to have the potential to induce carbonate precipitation in concretions are (1) dissimilatory ferric iron reduction, (2) bacterial sulfate reduction, and (3) archaeal autotrophic methanogenesis. These processes can increase the pH or alkalinity. Characteristic isotopic signatures and molecular fossils (lipid biomarkers) of the prokaryotes involved in carbonate formation can be preserved in the carbonate matrix (e.g. Irwin et al., 1977; Coleman, 1985; Coleman et al., 1993; Duan et al., 1996; Kiriakoulakis et al., 2000; Pearson et al., 2005; Loyd et al., 2012a).

Regardless of the processes triggering cement formation, concretions only form in a confined zone of the sediment column. The equilibrium model suggests that an entire volume of sediment is uniformly supersaturated in carbonate and concretions form wherever appropriate nuclei occur (Coleman & Raiswell, 1995; Raiswell & Fisher, 2000). However, only few concretions with nuclei have been documented (Pye et al., 1990; Thomka & Lewis, 2013), whereas the majority of concretions lacks nuclei (e.g. Siegel et al., 1987; Coleman & Raiswell, 1995; Duck, 1995; Kiriakoulakis et al., 2000; Lash & Blood, 2004; Loyd et al., 2012a). An alternative model, the so-called dynamic or local-equilibrium model presumes a spatial variation in carbonate saturation, caused by localized diagenetic activity, which in turn results from a heterogeneous distribution of organic matter (Coleman, 1985; Coleman & Raiswell, 1995; Duck, 1995; Raiswell & Fisher, 2000). In some cases, where organic matter contents are minor (e.g. Lash & Blood, 2004), diffusion and fluid flow are alternative mechanisms for the formation of concretions (fluid-mixing model by Raiswell & Fisher, 2000).

Here, subspherical to elliptical calcite and siderite concretions with high carbonate contents from two locations in Eastern Austria were studied. The studied calcite concretions are from the sandpit of Steinbrunn (Čáry Formation), in the southern Vienna Basin, which represents the transition from fully marine to limnic conditions during the Pannonian, around 10 Ma ago (Grundtner et al., 2009; Wieninger et al., 2009). The host sediment of the studied siderite concretions comprise sandy to silty turbidites in the

Gosau Basin of Gams, northern Styria. The basin is part of the Northern Calcareous Alps and belongs to the Upper Gosau Subgroup, which reflects a marine deep water environment. The siderite concretions were found, together with entire layers of siderite, in sections around the Paleocene-Eocene boundary, 55 Ma ago, which form part of the Zwieselalm Formation (Wagreich et al., 2011). The current work emphasis on the factors steering growth geometry and the mechanisms of carbonate precipitation. It particularly tries to shed light on the biogeochemical processes and types of prokaryotes involved.

# 2 Geological setting

## 2.1 Sandpit Steinbrunn

The sandpit of Steinbrunn (Fig. 1) in Burgenland close to the border to Lower Austria consists of calcareous sands, silts, clays and detrital limestones of the Vienna Basin and its continuation into the Eisenstadt Basin (Grundtner, 2009; Grundtner et al., 2009; Wieninger, 2009). The northeast-southwest striking Vienna Basin is a rhombe-shaped pull-apart basin that is about 200 km in length and 50 km in width, located between the Eastern Alps, the Western Carpathians and the Western Pannonian Basin (Piller et al., 1996; Wessely, 2006; Grundtner et al., 2009). The basin developed in the Miocene and was filled by sediments of the Central Paratethys Sea, ranging from the Karpatian to the Pannonian (Table 1; see also Piller et al., 1996; Faupl, 2003; Wessely, 2006; Grundtner, 2009; Grundtner et al., 2009; Wieninger, 2009).

The sandpit of Steinbrunn comprises unconsolidated sediments of Pannonian age (11.6 – 7.1 Ma), belonging to the Lower Neufeld beds or Čáry Formation (Grundtner et al., 2009; Wieninger, 2009; Fig. 2). While during the Badenian and Sarmatian the Vienna Basin was fully marine, it was consecutively separated from the Paratethys in the Pannonian and transformed into the brackish, later limnic Pannonian Lake (Piller et al., 1996; Faupl, 2003; Wessely, 2006; Grundtner et al., 2009; Wieninger, 2009). The Steinbrunn sandpit deposits represent this brackish-limnic stage, but also contain reworked, detrital marine limestones of the Badenian, so-called "Leithakalk" with abundant corallinaceans and bryozoans. A detailed profile (Fig. 3), ranging from ca. 10.1 to 9.9 Ma, shows a coarsening and shallowing upward trend (Grundtner et al., 2009). The lowermost section, called unit A, comprises 6 m of laminated clays and silts with carbonate contents around 20 wt.% (Grundtner et al., 2009). Unit A contains chiefly quartz, calcite, dolomite, but also minor feldspar, muscovite and the clay minerals smectite and chlorite. The clays and silts are light brown to dark gray in color, and contain bitumen. Grundtner et al. (2009) classified the section as deposits of a local brackish-limnic pond. Carbonate concretions were found exclusively in this unit (Grundtner et al., 2009). Unit B is the thickest unit, comprising 14 m of sediments, which show, compared to unit A, coarser grain sizes and considerably higher carbonate contents of 80 wt.% on average. It consists of poorly sorted detrital limestones and carbonate sands, rhythmically intercalated with clays and marls. The carbonate clasts are sourced from the reworked Leithakalk deposits (Grundtner et al., 2009). The uppermost part of the profile, unit C, has a thickness of 4 m and carbonate contents at around 80 wt.% for the coarse sands, and around 76 wt.% for the fine sands. Unit C represents the coarsest grain sizes of the section with fine gravel, detrital limestones, coarse- to medium-grained carbonate sands and rip-up clasts of light gray clay. The gravel as well as the clay clasts are both reworked Badenian sediments. Channel

structures with erosive base and cross-beddings occur, which have been interpreted as flood plain deposits by Grundtner et al. (2009). Within the entire section carbonate content and grain size correlate positively, the coarser the sediment, the higher the carbonate content (Grundtner et al., 2009).
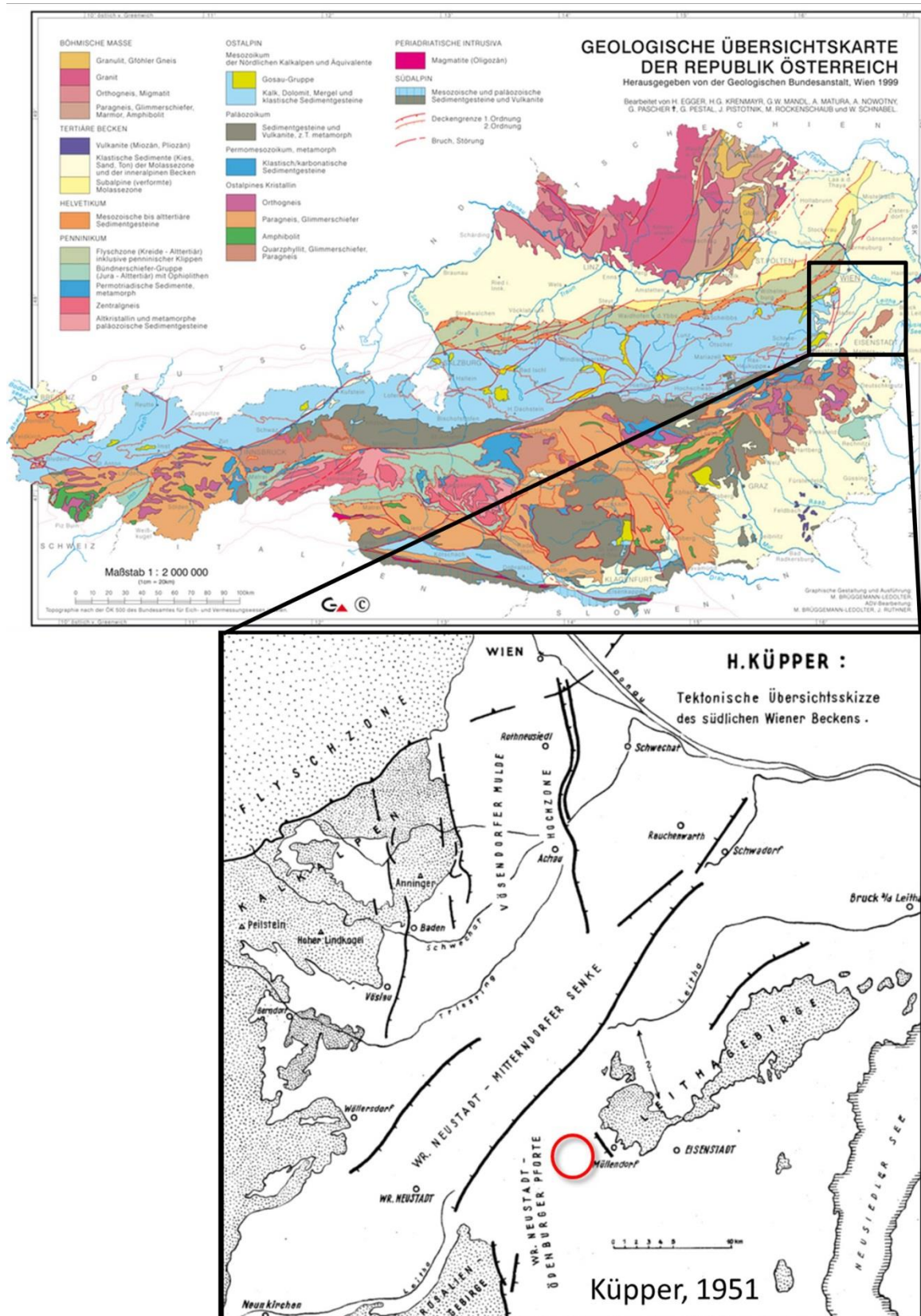
Fig. 1: Location of the sandpit of Steinbrunn; Geological map of Austria, modified from Geologische Bundesanstalt (Vienna, 1999); framed section: Geological map of the Vienna Basin indicating the sandpit of Steinbrunn in the center of the red circle, modified from Küpper (1951).

| M.A. | EPOCH | AGE | CENTRAL PARATETHYS STAGES | EASTERN PARATETHYS STAGES | BIOZONES Berggren et al., 1995 | |
|---|---|---|---|---|---|---|
| | | | | | Planktonic Foraminifera | Calcareous Nannoplankton |
| 5 | PLIO-CENE | ZANCLEAN | DACIAN | KIMMERIAN | PL1 | NN13 |
| 5.3 | Late MIOCENE | MESSINIAN | PONTIAN | PONTIAN | M14 | NN12 |
| | | TORTONIAN | PANNONIAN | MAEOTIAN | M13 b | NN11 |
| 10 | | | | | M13 a | NN10 |
| | | | | | | NN9b |
| 11.0 | | | | SAR-MATIAN Khersonian | M12 | NN9a/8 |
| | Middle MIOCENE | SERRAVALLIAN | SARMATIAN | Bess-arabian | M11-M8 | NN7 |
| | | | | Volhynian | | NN6 |
| 15 | | | BADENIAN | Konkian Karaganian Tshokrakian | M7 | NN5 |
| | | LANGHIAN | | TARKHANIAN | M6 / M5 | |
| 16.4 | | | KARPATIAN | KOTSAKHURIAN | M4 | NN4 |
| | Early MIOCENE | BURDIGALIAN | OTTNANGIAN | | M3 | NN3 |
| 20 | | | EGGENBURGIAN | SAKARAULIAN | M2 | NN2 |
| | | AQUITANIAN | EGERIAN | CAUCASIAN | M1 b | |
| 23.8 | | | | | M1 a | NN1 |

Table 1: Stages of the Central Paratethys in comparison with international nomenclature; from Piller et al. (1996).



Fig. 2: Overview of the sandpit of Steinbrunn in a westward direction; from Grundtner (2009).
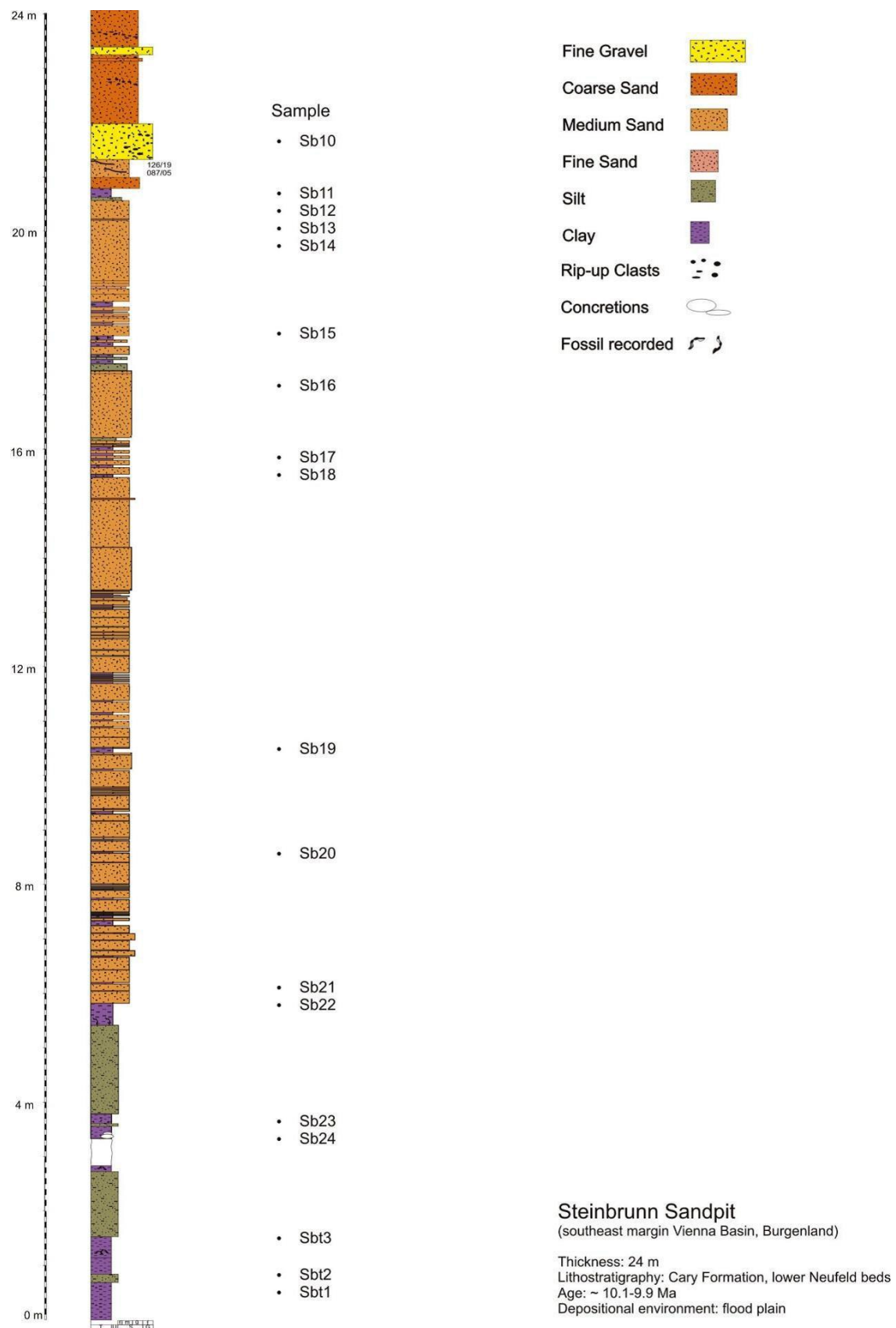
Fig. 3: Profile of the sandpit of Steinbrunn; from Grundtner (2009).

## 2.2 Gosau Basin of Gams

Sandy to silty, turbidite-dominated deposits with thin layers and concretions of siderite crop out in the Basin of Gams, in northern Styria, east of the Enns valley, and belonging to the Northern Calcareous Alps (Fig.4). The section is part of the Zwieselalm Formation of the Upper Gosau Subgroup (Wagreich et al., 2011). The Gosau Group is composed of sediments lying unconformably upon parts of the Calcareous and Central Alps, which suffered extensive folding and thrusting by the Early Cretaceous orogenesis (Faupl, 2003; Wagreich et al., 2011). The sediments were deposited in the northwestern Tethyan realm in a regime formed by transtension and further subsidence (Wagreich et al., 2011). The so-called "Gosau sea" gradually inundated the Austro-Alpine microplate from the north (Faupl, 2003; Wagreich et al., 2011). First, the Northern Calcareous Alps received sediment from the accretionary wedge of the subducting Southern Penninic ocean in the north, as well as the Tethys suture in the south. From the Maastrichtian on, sediment delivery changed and the southern metamorphic units of the Austroalpine became the only source region (Faupl, 2003). The Gosau Group developed from a subtropical, terrestrial to shallow water environment (Lower Gosau Subgroup) in the Late Turonian to Campanian to a deep water sedimentary environment (Upper Gosau Subgroup) from the Campanian to Ypresian (Faupl, 2003; Wagreich et al., 2011).

In the Gosau Basin of Gams both the Lower and the Upper Gosau Subgroup are exposed. The Upper Gosau Subgroup is represented by the Nierental and the Zwieselalm Formation (Wagreich et al., 2011). The Zwieselalm Formation reaches from the Danian to the Ypresian, with siderite concretions and layers placed around the Paleocene-Eocene boundary (55 Ma), ranging from ca. 56 to 54.5 Ma. The Zwieselalm Formation is primarily composed of turbidites, whereas the underlying Nierental Formation (Campanian to Danian) represents the facies of the basin slope, consisting of pelagic marls and marly limestones with intercalated thin turbidites (Faupl, 2003; Wagreich et al., 2011). The section studied by Wagreich et al. (2011), the so-called Pichler section, comprises 122 m of the Zwieselalm Formation at the Paleocene-Eocene-boundary, and it contains the early diagenetic siderite. This part is dominated by psammitic to pelitic turbidites, either carbonate-free or with distinctive marl layers (Fig.5). Wagreich et al. (2011) distinguished between two facies types, a carbonate-bearing coarser grained and an almost carbonate-free, finer grained facies, whereas the boundaries in-between these facies are rather ill-defined. The lowermost 13 m of the profile represent the carbonate-bearing facies with a fining-upward sequence from gravel-dominated to fine-sandstone/siltstone turbidites and turbiditic marl layers as well as dark gray, mainly carbonate-free, turbiditic shales. Bioturbation has been observed in some parts of the section (Wagreich et al., 2011). Marl beds are absent in the middle part of the section, between meter 13 and 80. This part is composed of thin-bedded sandy- to silty turbidites, thin, dark gray silty claystone intervals and thin layers and concretions of siderite. The siderite concretions are embedded within sandy-silty as well as in silty-clayey material.

The dark claystones contain 0 to 6.4 wt.% carbonate (Wagreich et al., 2011). From meter 0 to 80 complete Bouma sequences have been recognized within thicker beds (Wagreich et al., 2011). The uppermost section reveals also siderite concretions, the highest carbonate contents (av. 19.7 wt.% in marl layers), convolute bedding and other water-escape structures within thick sandstone beds. Generally, Wagreich et al. (2011) assumed high sedimentation rates of approximately 20 cm/kyr for these turbidite successions.
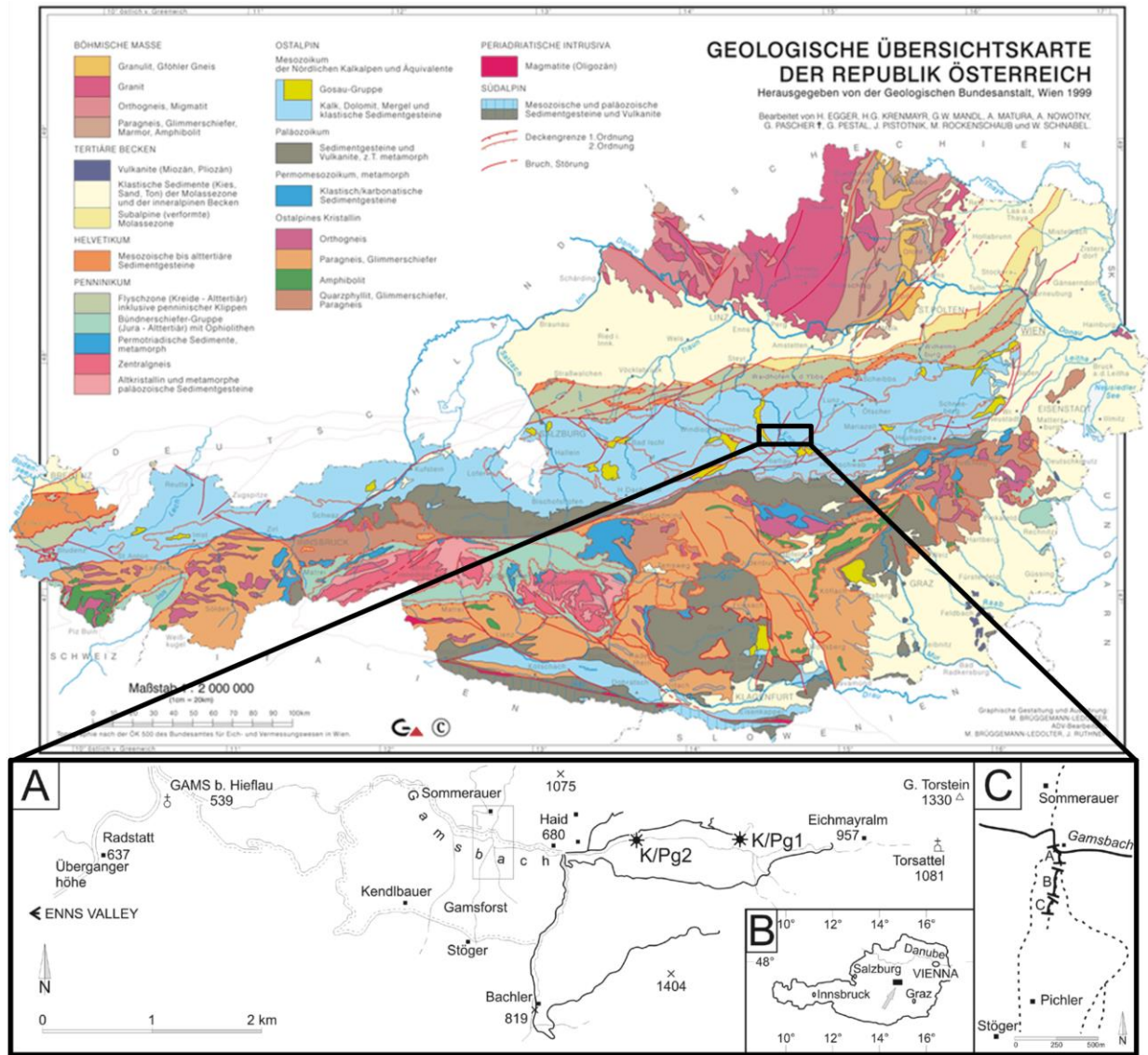


Fig. 4: Location of the Gosau basin of Gams; Geological map of Austria, modified after Geologische Bundesanstalt (Vienna, 1999); framed section: A: Sketch map of the Gams area indicating the investigated section in a southern unnamed tributary creek of the Gamsbach; B: Inset map of Austria and location of Gams sections; C: Sketch map indicating detailed location of the investigated sections; modified after Wagreich et al. (2011).
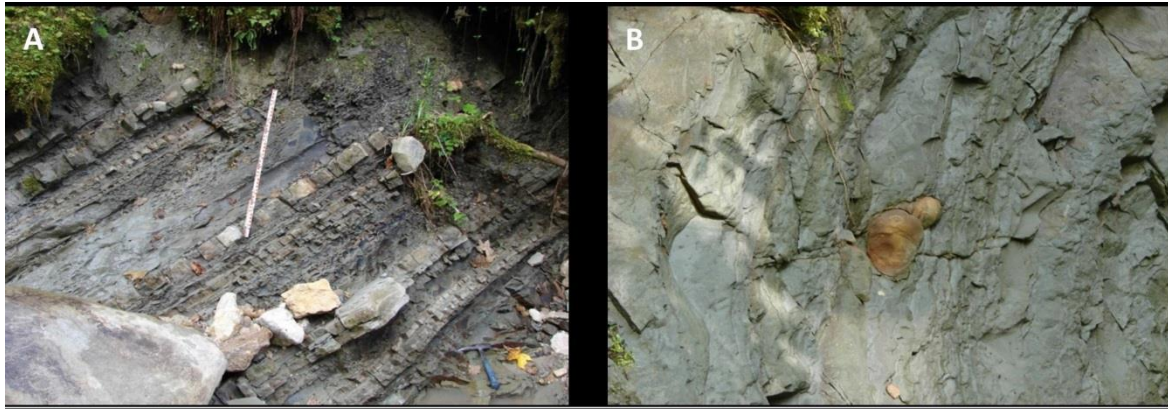
Fig. 5: Photos of the Pichler section (Zwieselalm Fm.); A: Psammitc to pelitic turbidites with intercalated marl and siderite layers; B: Siderite concretion embedded in its host rock, a pelitic turbidite; from Wagreich et al. (2011).

# 3 Materials and Methods

If not further specified, all measurements have been carried out at the Department of Geodynamics and Sedimentology, University of Vienna.

## 3.1 Materials

Ten calcite concretions from Steinbrunn and three siderite concretions from the Gams locality plus the respective host rocks were examined (Table 2). Calcite concretions, which were found washed out of the sediment, are labeled with "F" or "Fu", whereas those found within the sediment are labeled with "G". S1_12 ("S" for "sandstone") represents the ambient sediment. GAMS1_12 is the host rock of the siderite concretions. GAMS2_12, GAMS3_12 and GAMS4_12 are siderite concretions. Table 2 gives an overview of the methods applied on each concretion or host rock sample. Calcite concretions are oblate, sometimes elongated and in one case, dumbbell-shaped, bodies. Their height ranges from 3 to 10 cm, their width from 4 to 20 cm and their length from 10 to 37.5 cm (Fig. 6A–G). Siderite concretions are of platy to rounded shape, but not elongated (Fig. 7A–E). The height of the three concretions is 5, 7 and 9 cm respectively and the diameter is approximately 16 to 17 cm for all three.

## 3.2 Thin sections

Uncovered thin sections were prepared and studied with an optical Leica DM 2700 P microscope using plane-polarized as well as cross-polarized light and the magnifications 25, 100, 200 and 630. Images were taken with this microscope equipped with a Leica MC170 HD camera. To identify the different carbonate minerals, thin sections F3_12, Fu1_12, G1_12, S1_12, GAMS2_12 and GAMS3_12 were stained with alizarin red S and potassium ferricyanide as described by Dickson (1965). For quantitative graphic evaluation of carbonate content from thin section photos the image processing and analysis software "ImageJ" was used. The taxonomy of foraminifera follows Rupp (1986) and Loeblich & Tappan (1987).

## 3.3 Bulk rock elemental analysis

Chemical composition of the siderite concretions and their host rock are from Wagreich et al. (2011). Carbon and sulfur contents were measured with a Leco CS200 as carbon dioxide and sulfur trioxide. Contents of cations, given as metal oxides, were determined

using the X-ray fluorescence device Spectro X-LAB 2000. Both analyses were carried out at the Geological Survey (Geologische Bundesanstalt) in Vienna.

## 3.4 Müller-Gastner carbonate bomb

Carbonate contents of concretions and their ambient sediments were determined by using the carbonate bomb after Müller & Gastner (1971). Per measurement 700 mg of powdered sample, generated with a handheld micro-drill, were dissolved with concentrated hydrochloric acid in a cylindrical jar with a manometer calibrated in percent of calcium carbonate. The underlying principal is that the created carbon dioxide pressure when dissolving the carbonate is proportional to the amount of calcium carbonate in the sample. The resulting carbonate contents shall be understood as weight percent.

## 3.5 Powder X-ray diffraction

Mineralogical composition of one sample, the calcite concretion G4_12, was analyzed by powder X-ray diffraction (XRD). The sample was loaded in the sample holder (monocrystalline silicon) as oriented powder and was analyzed with a Panalytical X'Pert PRO diffractometer (CuKα radiation, 40 kV, 40 mA, step size 0.0167, 5 s per step). The X-ray diffraction patterns were interpreted using the Panalytical software "X'Pert High score plus".

## 3.6 Stable isotope measurements

Samples were taken from slabs of the concretions and the host rock samples using a handheld micro-drill. Analysis has been carried out at the University of Graz using the procedure as described in Heindel et al. (2015). The powdered samples were dissolved in 100% phosphoric acid in a Kiel II automated reaction system at 70°C. The resulting carbon dioxide gas was analyzed in a Finnigan Delta Plus mass spectrometer with a precision better than 0.05‰ for $\delta^{13}C$ and 0.1‰ for $\delta^{18}O$ values. The $\delta$ values are corrected according to the NBS19 standard and reported in per mill (‰) relative to the Vienna-PeeDee Belemnite (V-PDB) standard. All $\delta^{13}C$ and $\delta^{18}O$ values mentioned in the text refer to this standard.

The $\delta^{18}O$ values of siderite have been corrected for the sake of comparison with calcite values. The fractionation factors of calcite-water and siderite-water have been calculated using the equation of Zheng (1999):

$$10^3 \ln\alpha = A \times 10^6/T^2 + B \times 10^3/T + C$$

Whereas first, the A, B and C values for calcite-water were used and the second time the equivalent values for siderite-water:

|               | A    | B     | C    |
|---------------|------|-------|------|
| calcite-water | 4.01 | –4.66 | 1.71 |
| siderite-water| 4.23 | –4.58 | 1.73 |

After this, the difference between the two fractionation factors was calculated and this value was substracted from each of the $\delta^{18}O$ values of siderite. As there is very little fractionation of carbon isotopes during precipitation and dissolution reactions (Loyd et al., 2014), no correction of $\delta^{13}C$ values was made.


## 3.7 Extraction and analysis of lipid biomarkers from carbonate rocks

The method used for extracting lipid biomarkers from calcite and siderite concretions is similar to the method introduced by Birgel et al. (2006), which is a modified method as introduced by Bligh & Dyer (1959). Further, an extraction-dissolution-extraction procedure as introduced by Arning et al. (2009) for phosphorites was applied. Hoffmann-Sell et al. (2011) used a very similar technique for lipid extraction of dolomite concretions and background sediment.

The material was first cleaned with hexane and dichloromethane (DCM) to exclude contaminations on the surfaces. Then the sample was broke up and powdered with hammer and mortar, respectively. 100 g of rock for each sample was powdered on average. For quantification three internal standards were added, 5-α-cholestane for hydrocarbons, 1-nonadecanol for alcohols and 2-Methyl-$C_{18}$ fatty acid for the fatty acid fraction, usually 10 µg of each. The powder was mixed with an organic solvent mixture (DCM: methanol 3:1) to extract the organic compounds. The organic solvent mixture was separated from the powder by centrifugation and was decanted and collected in a separatory funnel. This procedure was repeated two to three times, at least until the extract became colorless. The pooled lipid extracts were treated with deionized, DCM-cleaned water and then separated into an organic and an aqueous phase. The organic phase was dried with sodium sulphate in a funnel and then reduced in the rotation evaporator to receive a dry total lipid extract. This first extraction procedure contains biomarkers not tightly bond to the carbonate matrix. The extracted carbonate powder was dissolved with 10% hydrochloric acid to aim for compounds enclosed within the carbonate matrix. Calcite was dissolved at room temperature, whereas siderite was dissolved at 47°C. After digesting the carbonate until ca. 80% of the carbonate was dissolved, the solution was centrifuged and the supernatants were decanted and discarded as explained above. The resulting solid material was then saponified to release carboxylic acids, and after that, the supernatants of this saponification were collected in a separatory

funnel. The organic solvent mixture (see above) was mixed with the residual powder after decalcification and saponification and the resulting, extracted organic compounds were added to the supernatants of the saponification. Again, the pooled extracts were cleaned with water, but 10% hydrochloric acid was further added until pH=2 was reached, to release the carboxylic acids from the aqueous phase into the organic phase.

The DCM-soluble asphaltenes were separated from the *n*-hexane soluble maltenes to receive cleaner extracts and a better separation and less background on the gas chromatograph. The maltenes were further separated by solid-phase column chromatography, with an SPE-aminopropyl silica gel column. By using solvents with increasing polarity, the total extracts were divided into four fractions: hydocarbons (4 ml *n*-hexane), ketones (6 ml *n*-hexane:DCM 3:1), alcohols (7 ml DCM:acetone 9:1) and fatty acids (8 ml 2% formic acid in DCM). The alcohol fraction was derivatized to trimethylsilyl ethers by reacting with bis(trimethylsilyl)-trifluoroacetamide and pyridine. The fatty acid fraction was derivatized to fatty acid methyl esters with boron trifluoride. Derivatisation of the polar fractions was necessary in order to avoid adherence to the stationary phase of the GC column. It made the fractions less polar and more volatile.

Measurements were carried out using a gas chromatograph equipped with a flame ionization detector (GC-FID), an Agilent 7820 A GC system, for quantification. For identification, all samples were measured on a GC linked to a quadrupole mass spectrometer (GC-MS), an Agilent 7890 A GC system coupled to an Agilent 5975 C inert MSD mass spectrometer. Both GC-FID and GC-MS used helium as carrier gas and were equipped with a 30 m HP-5 MS UI fused silica capillary column (0.25 mm in diameter, 0.25 μm film thickness). The GC temperature program was as follows: 60 °C (1 min); from 60 °C to 150 °C at 10 °C/min; from 150 °C to 320 °C at 4 °C/min, 25 min isothermal for all fractions. Interpretation of gas chromatograms was made with "Agilent MSD Productivity ChemStation for GC and GC/MS Systems Data Analysis Application" software. Quantification of compounds was done by comparing peak areas with the internal standards added prior extraction, whereas identification was based on retention times and comparison with the NIST database and published spectra, available in Agilent ChemStation software and in the literature.

| Nr. | Name | Locality and type | Thin section | Carbonate | Isotopes | Biomarker |
|---|---|---|---|---|---|---|
| 1 | F1_12 | Steinbrunn concretion | | | | |
| 2 | F2_12 | Steinbrunn concretion | | | | |
| 3 | F3_12 | Steinbrunn concretion | Yes/stained | 86% | 2 | |
| 4 | F4_12 | Steinbrunn concretion | Yes | 86% | 2 | Yes |
| 5 | Fu1_12 | Steinbrunn concretion | Yes/stained | 84% | 5 (profile) | |
| 6 | Fu2_12 | Steinbrunn concretion | | 85.5% | | |
| 7 | G1_12 | Steinbrunn concretion | Yes/stained | 85.5% | 2 | |
| 8 | G2_12 | Steinbrunn concretion | Yes | | 2 | |
| 9 | G3_12 | Steinbrunn concretion | | | | |
| 10 | G4_12 | Steinbrunn concretion | Yes | | 2 | Yes |
| 11 | S1_12 | Steinbrunn host rock | Yes/stained | 83.5% | 4 (profile) | |
| 12 | GAMS1_12 | Gams host rock | | 34% | | |
| 13 | GAMS2_12 | Gams concretion | Yes/stained | 72.5% | 6 (profile) | Yes |
| 14 | GAMS3_12 | Gams concretion | Yes/stained | 80%/45% | 2 | |
| 15 | GAMS4_12 | Gams concretion | Yes | 81.5% | 2 | Yes |

Table 2: List of all samples. "Yes"= thin section was made/lipid biomarkers were analysed; carbonate contents are given in % according to Müller-Gastner or thin section graphical analysis; values in the "Isotopes" column are number of subsamples taken.

# 4 Results

## 4.1 Macroscopic description

### 4.1.1 Steinbrunn calcite concretions

The color of the calcite concretions is mostly light yellowish to grayish with red brown patches of iron oxyhydroxides. Interestingly, the darker and grayer specimen Fu1_12 (Fig. 6A) contains more pyrite than the other calcite concretions from which thin sections were taken (see below). A conspicuous feature of all calcite concretions are the septarian cracks. The septarian cracks are not filled, but some show beginning growth of cement on crack walls. Orientation of cracks is dominantly vertical (Fig. 6E). Horizontal sections show a polygonal pattern in the center and (Fig. 6C and 6F) a preferred orientation along the length of the concretion in the more marginal zones. Septarian cracks are widest in the center, and narrowing towards concretion margins. The crack tips normally do not reach the surface. According to Astin (1986), this crack pattern is quite common for concretions with such a regular shape. The host sediment is a slightly darker and little more yellowish silt and clay with fine sand (Fig. 6H). It seems that the secondary calcite causes the light color of the concretions.
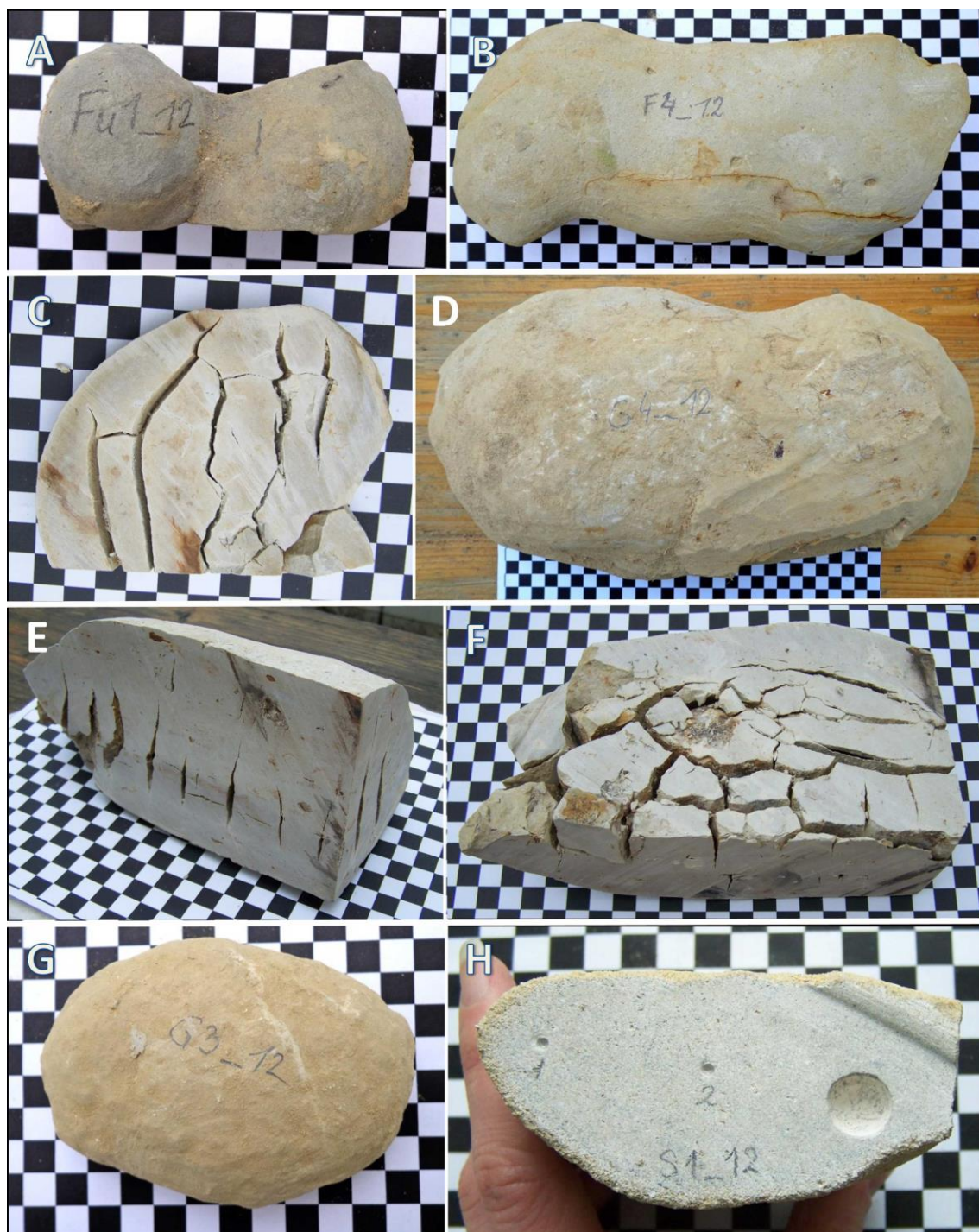
Fig. 6: Photographs of selected Steinbrunn calcite concretions and their host rock. One square equals one square centimeter. A: Calcite concretion Fu1_12, length: 10 cm. B: Calcite concretion F4_12, length: 27 cm. C: Horizontal section of calcite concretion F4_12, septarian cracks parallel to elongation are visible. D: Calcite concretion G4_12 with residual sediment cover, length: 37.5 cm. E: Two vertical sections of calcite concretion G4_12, vertically oriented septarian cracks are visible. F: Horizontal section of calcite concretion G4_12, polygonal crack pattern and cracks parallel to elongation are visible. G: Calcite concretion G3_12 with residual sediment cover, length: 11.5 cm. H: Host rock S1_12, the two small holes are the spots where material for isotope analysis was taken, the large hole marks the site, where material for carbonate content analysis was removed.

## 4.1.2 Gams siderite concretions

The concretions are of reddish brown, rusty color, but there are usually lighter and darker zones caused by bioturbation. GAMS3_12, for example, has a paler and softer core (Fig. 7A and B). The host sediment of the siderite concretions is a grayish to yellowish mudstone (Fig. 7F).



Fig. 7: Photographs of selected Gams siderite concretions and their host rock. One square equals one square centimeter. Small holes are the spots where material for isotope analysis was taken, the large holes mark the sites, from which material for carbonate analysis was removed. A: Interior of siderite concretion GAMS3_12, with gray host rock material at the bottom, soft, pale core with rough surface, diameter: 17 cm. B: Vertical section of siderite concretion GAMS3_12, soft, pale core with rough surface. C: Half of siderite concretion GAMS4_12, diameter: 16 cm. D: Vertical section of siderite concretion GAMS2_12, diameter: 16 cm. E: Siderite concretion GAMS2_12 cut in two pieces. F: Host rock GAMS1_12.

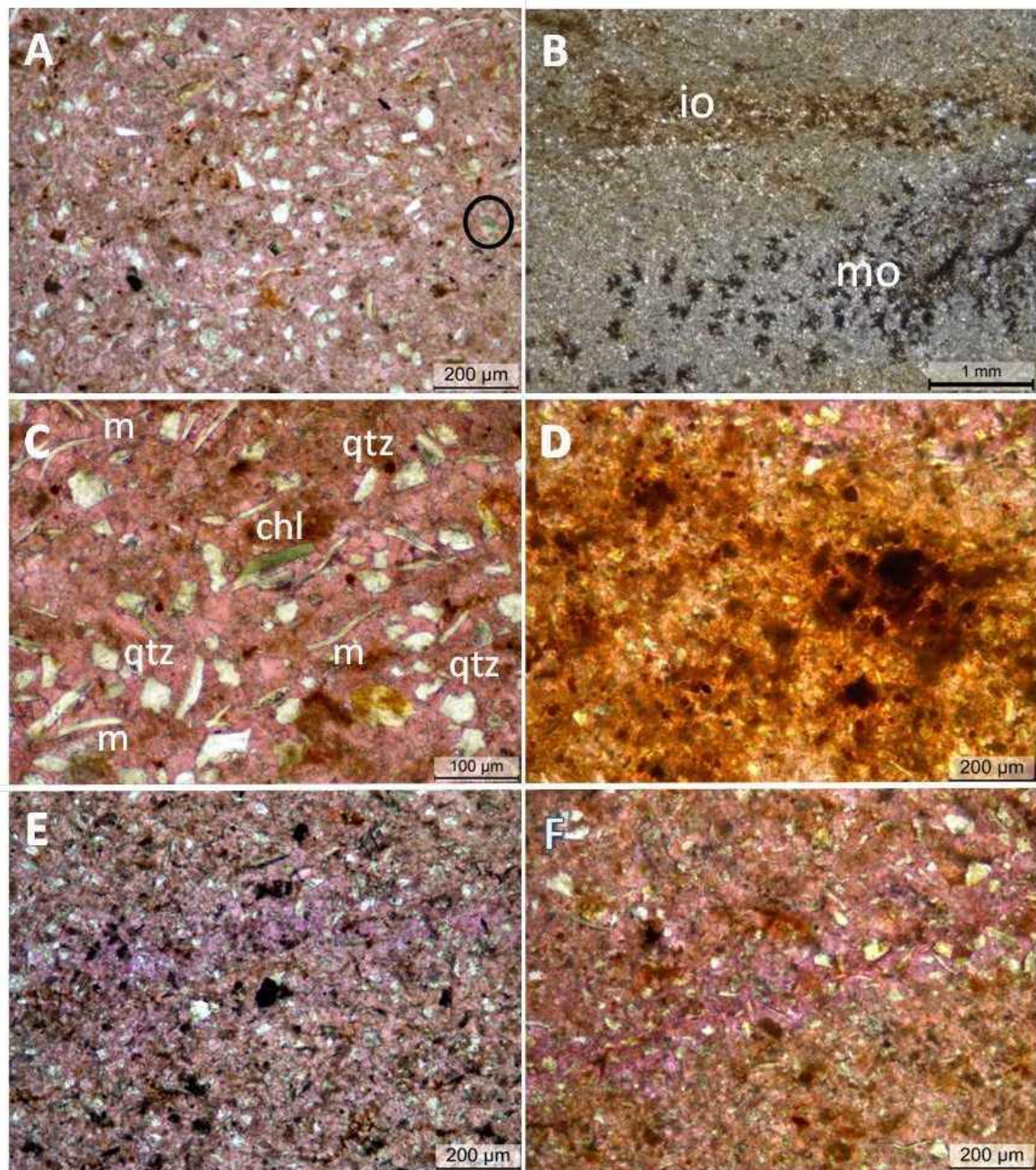## 4.2 Petrography

### 4.2.1 Steinbrunn calcite concretions



Fig. 8: Micrographs of Steinbrunn calcite concretions; pink: calcite; purple: ferroan calcite; white: detrital quartz, mica and authigenic dolomite; black: iron oxyhydroxides or pyrite; reddish brown: oxidation rims of opaque minerals; black circle: chlorite. chl: chlorite; io: iron oxyhydroxides; m: mica; mo: dendritic manganese oxides pl: plagioclase, qtz: quartz. A: Calcite concretion F3_12 in plane-polarized light; stained; typical appearance of a calcite concretion; ev. authigenic dolomite. B: Calcite concretion G1_12 in plane-polarized light; typical calcite concretion. C: Calcite concretion Fu1_12 in plane-polarized light. D: Calcite concretion G1_12 in plane-polarized light; oxidized zone with abundant iron oxyhydroxides, probably oxidized pyrite; and authigenic dolomite. E: Calcite concretion Fu1_12 in plane-polarized light; band of stronger ferroan calcite from the left to the right. F: Calcite concretion G1_12 in plane-polarized light; band of stronger ferroan calcite from the lower left to the upper right corner.

Concretionary cement occurs as micrite and sparry calcite crystals, the latter representing so-called microspar (Fig. 8A–F). The crystal size distribution is rather heterogeneous and ranges from 5 to 50 µm, a crystal size typical for calcite concretions (Raiswell & Fisher, 2000). Fluctuations of grain size seem to be an effect of bioturbation or primary sedimentary layering. It cannot be excluded that parts of the calcite are detrital. Indeed, it seems quite likely considering the calcareous nature of the host rock. Nevertheless, the methods used in this study could not differentiate between authigenic and detrital calcite. Beside calcite the concretions contain quartz, muscovite, chlorite (Fig. 8A and 8C), plagioclase, K-feldspar, iron oxy hydroxides, manganese oxides (Fig. 8B, 8D and 8F), authigenic dolomite (Fig. 9C, the rhombic crystal shape indicates authigenic formation) and fossils. Kerogen or plant debris occur in various calcite concretions (Fig. 8B). The iron content is also heterogeneous in the calcite concretions, apparent from bands of purple calcite (higher iron content) within more pinkish calcite in stained thin section (Fig. 8E and 8F). Pyrite was observed in various samples and is apparently of an authigenic origin based on the occurrence of framboidal crystal aggregates (Fig. 9A and 9B). It occurs in at least three calcite concretions, F4_12, G4_12 and Fu1_12, and is especially abundant in the latter (Fig. 9A). As Fu1_12 and Fu2_12 show the same color, it is very likely that Fu2_12, from which no thin section exists, also contains abundant pyrite, probably, framboidal pyrite. Septarian cracks occur in all calcite concretions. The cracks are not filled with cement, but most of them show beginning cementation to various degrees. Concretions F4_12 and G4_12, reveal almost no cementation (Fig. 9D), concretion G1_12 occupies an intermediate state and F3_12 and G2_12 exhibit the most advanced infilling of the cracks, which contain dog-tooth cements (Fig. 9C, 9E and 9F). The opposite, oxidation around a crack was also observed, as for example in calcite concretions F3_12 and G1_12.

All of the calcite concretions and their host rock contain fossils (Fig. 10). In the concretions the fossil inventory is dominated by ostracodes. Fig. 10A shows a structure, which eventually could be also a small bivalve shell, but due to the size it is more likely that it is as well an ostracode. In calcite concretions F3_12 and G4_12 structures have been found, which are also ostracode shell fragments. The brownish to yellowish structures form the typical shape of these organisms (Fig. 10B). The most abundant fossils are fragments of corallinacean algae (Fig. 10C). However, foraminifera, such as *Bulimina* sp., *Rosalina* sp. and *Operculina* sp. are also rather abundant and also bryozoans were observed (Fig. 10D, 10E and 10F). Fossils make up more than 50% of this sandstone, beside them, minerals such as quartz (partly polycrystalline), muscovite, kaolinite and opaque phases were observed.
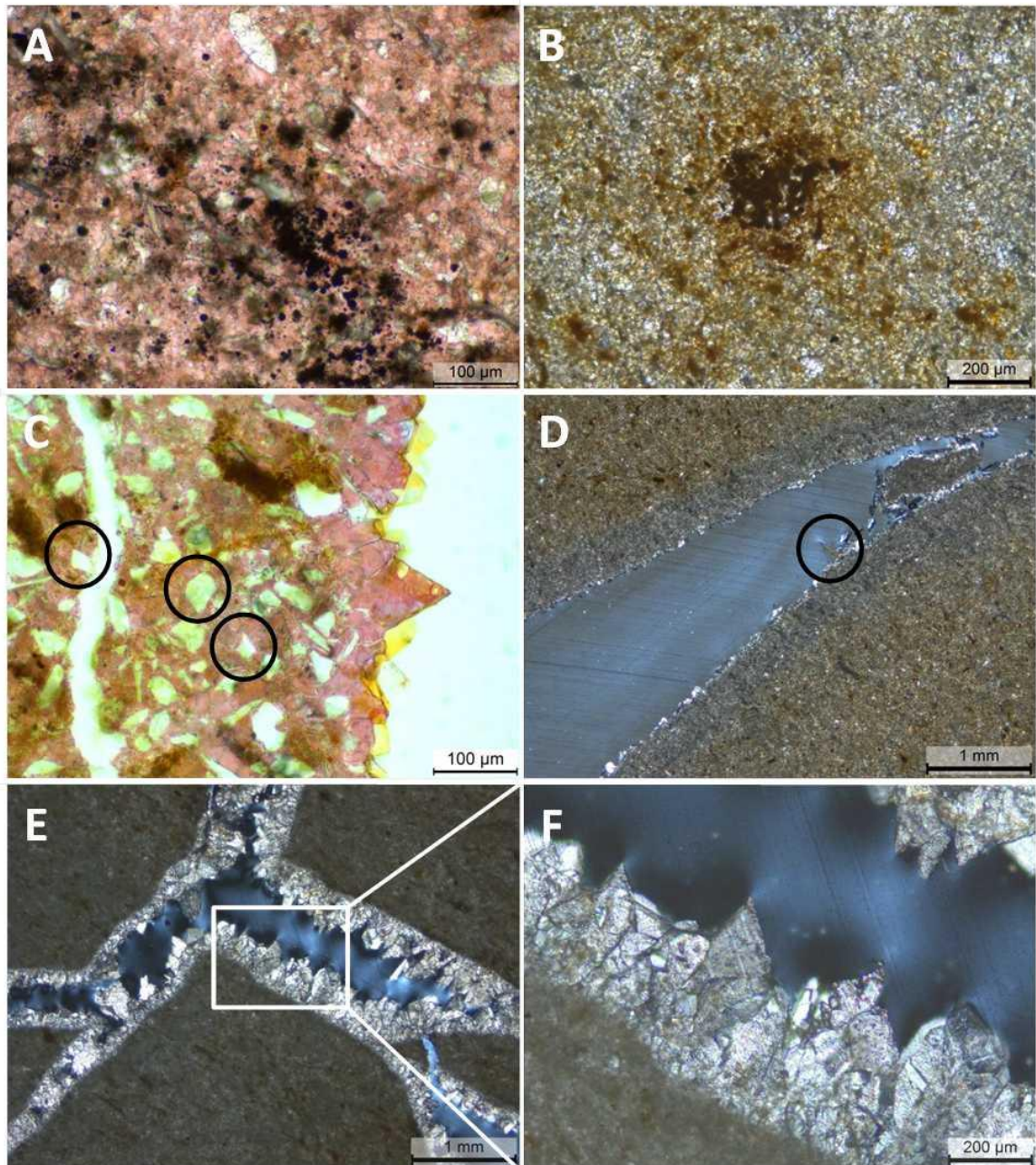
Fig. 9: Micrographs of Steinbrunn calcite concretions. A: Calcite concretion Fu1_12 in plane-polarized light; partially oxidized framboidal pyrite (black). B: Calcite concretion F4_12 in plane-polarized light; stained; abundant framboidal pyrite (black), detrital material (white). C: Crack wall of calcite concretion F3_12 in plane-polarized light, with dog-tooth cement; stained; pink: calcite; black circles: probably dolomite; further quartz, white mica. D: Septarian crack of calcite concretion F4_12 in cross-polarized light; few cement, black circle: needle-shaped mineral (probably oxalate); grayish reduction front around the crack; piece of concretion material within the septarian crack in the upper right corner. E: Calcite concretion F3_12 in cross-polarized light; septarian crack with dog-tooth cement. F: Enlarged section of E; dog-tooth cement in higher magnification.
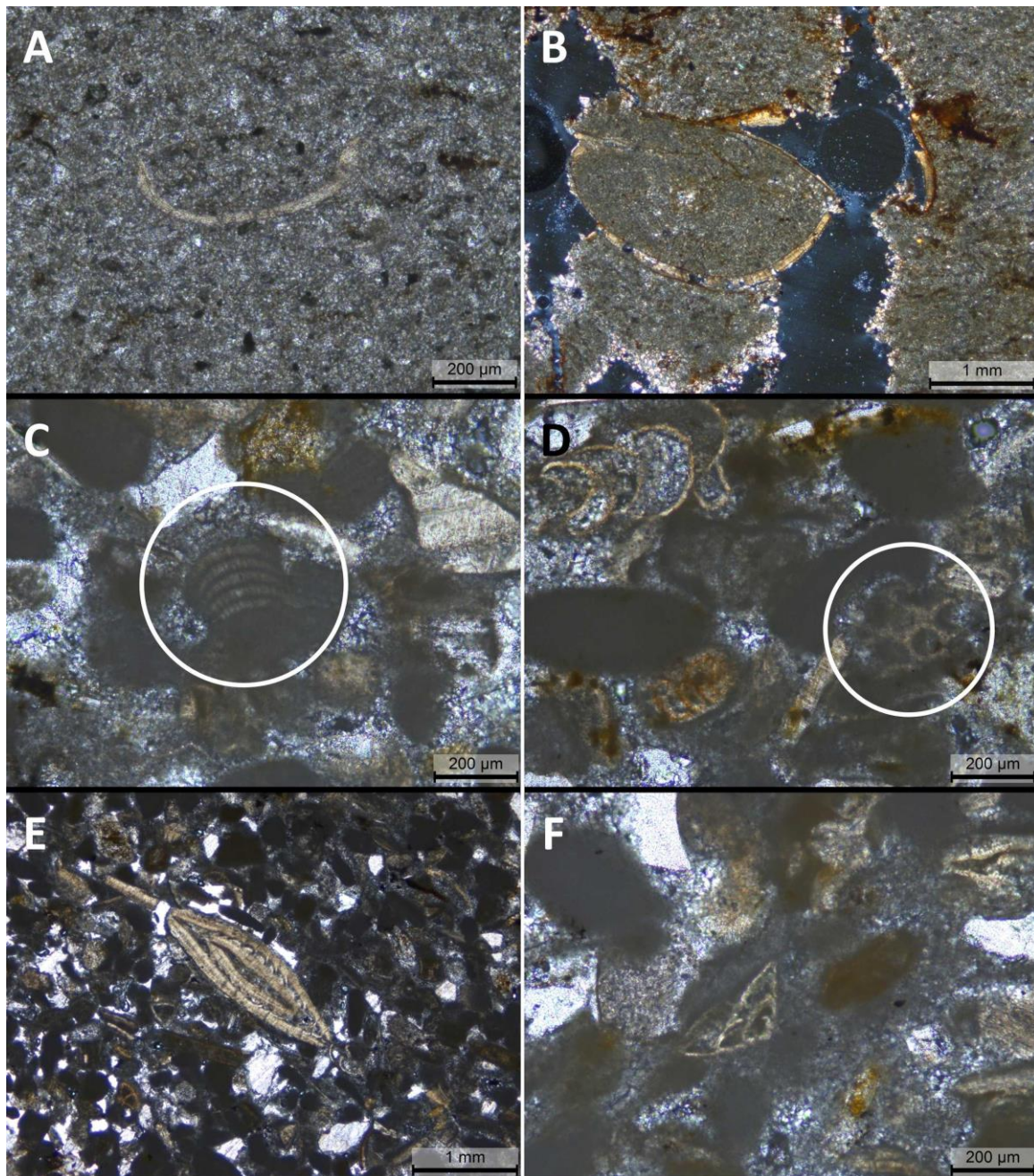
Fig. 10: Micrographs of Steinbrunn calcite concretions and their host rock. A: Calcite concretion Fu1_12 in plane-polarized light; one of two fossils found in this thin section, probably carapace of an ostracode or a small bivalve. B: Calcite concretion F3_12 in cross-polarized light, large ostracod carapace filled with concretionary material in the center. C: Calcareous sandstone S1_12 in plane-polarized light; white circle: corallinacean algae. D: Calcareous sandstone S1_12 in plane-polarized light; foraminiferum (*Bulimina* sp.) in the upper left corner; white circle: bryozoan fragment. E: Calcareous sandstone S1_12 in plane-polarized light; foraminiferum (*Operculina* sp.) in the center; black: fragments of corallinacean algae; white: detrital minerals; F: Calcareous sandstone S1_12 in plane-polarized light; foraminiferum (*Rosalina* sp.) in the center.

## 4.2.2 Gams siderite concretions
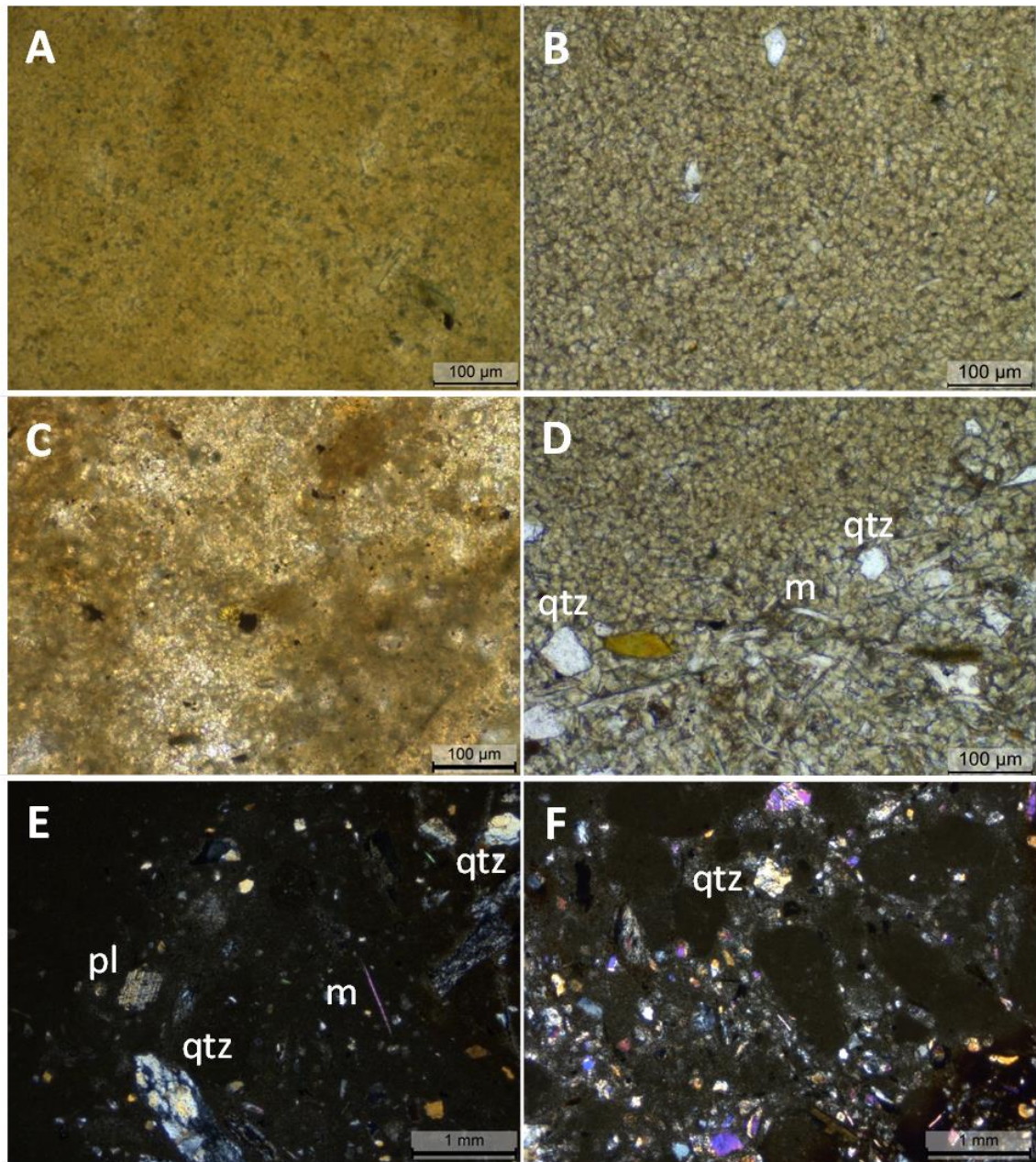


Fig. 11: Micrographs of Gams siderite concretions. A: siderite concretion GAMS3_12 in plane-polarized light; stained; homogenous zone of the concretion, very few detrital minerals, brownish: siderite; dark gray/blue: strongly ferroan calcite. B: siderite concretion GAMS2_12 in plane-polarized light; stained; saccharoidal siderite microspar with few detrital minerals. C: siderite concretion GAMS3_12 in plane-polarized light; saccharoidal siderite microspar with detrital and opaque minerals. D: siderite concretion GAMS2_12 in plane-polarized light; stained; upper left zone entirely microscopic sparry siderite, lower right zone: abundant detrital minerals. E: siderite concretion GAMS3_12 in cross-polarized light; plagioclase with polysynthetic twinning and polycrystalline quartz with oscillatory extinction. F: GAMS3_12 in cross-polarized light.

Similar to the calcite concretions the siderite concretions reveal carbonate microspar. However, also zones of coarse sparry siderite have been found and the cements occasionally appear saccharoidal (Fig. 11B and 11C). Siderite concretions comprise two carbonate minerals of significant amounts, siderite and strongly ferroan calcite. The two phases are clearly distinguishable in stained thin sections, where siderite appears light brown, whereas the calcite is colored blue, filling the residual pore volume between the siderite crystallites (Fig. 11A). Therefore, siderite predates the formation of ferroan calcite. To be precise, the concretions should be denominated as siderite-calcite concretions, but for the sake of simplicity are referred to as siderite concretions throughout. Detrital minerals of siderite concretions are quartz, plagioclase (Fig. 11E), muscovite (Fig. 11D, 11E and 12A), biotite, chlorite and kaolinite. The occurrence of pyrite is not proven, but suggested based on the occurrence of orange rims around opaque phases, which seem to be oxidation rims around pyrite (Fig. 12A). No fossils have been found in the concretions, but bioturbation. Quartz is generally clearly identifiable, in parts polycrystalline and shows oscillatory extinction, the typical features of metamorphic quartz (Fig. 11E and 11F). Nevertheless, also monocrystalline quartz with straight extinction (Fig. 12D) was found, which could imply mixed sources. Siderite concretions reveal a very heterogeneous distribution of siderite cement and siliciclastic material (Fig. 11D and 12C), coming along with a variation in color from dark brown to light orange (Fig. 12B), which is apparently enhanced by bioturbation and fluctuations in carbonate content. Especially GAMS3_12 reveals extensive bioturbation in its softer, paler and less cemented core. The bioturbation is visible, even macroscopically, as darker regions and as lenses of siliciclastic material, which are most likely infillings of burrows (Fig. 12C). Generally, no cracks occur within the siderite concretions, except for GAMS4_12, which has a crack filled with coarse sparry calcite, detrital quartz and an opaque phase, most likely authigenic pyrite (Fig. 12D).
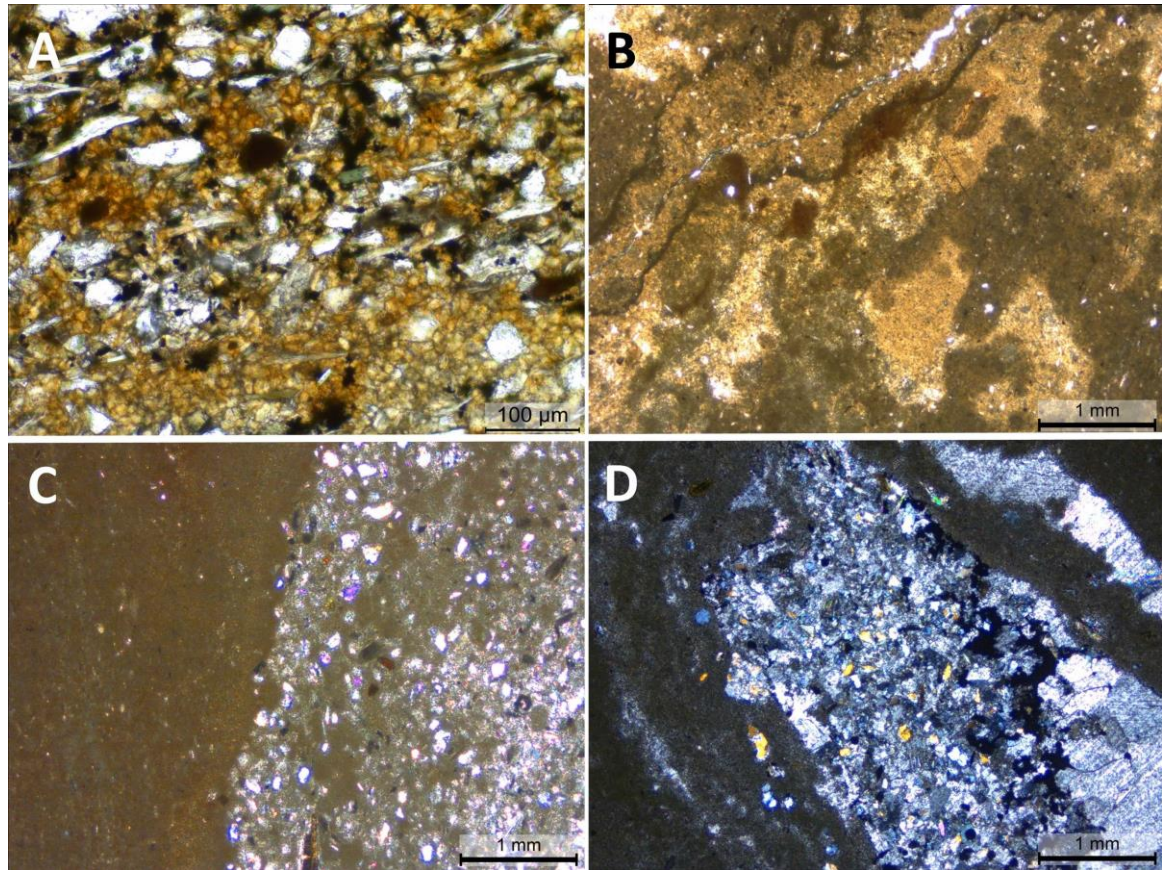
Fig. 92: Micrographs of Gams siderite concretions. A: siderite concretion GAMS2_12 in plane-polarized light; stained; orientation of micas, probably primary, sedimentary layering; white and elongated: mica; white isomorphic: quartz; brown: siderite; black: opaque minerals or kerogen. B: siderite concretion GAMS3_12 in plane-polarized light; patchy appearance, maybe due to fluctuations in carbonate content. C: siderite concretion GAMS3_12 in plane-polarized light; left side: concretion body mainly composed of siderite; right side: siliciclastic lens. D: siderite concretion GAMS4_12 in cross-polarized light; crack filled with coarse sparry calcite and quartz (yellow); quartz, mostly xenomorphic, some crystals are partially euhedral.

## 4.3 Bulk rock mineralogical and elemental analysis

### 4.3.1 Calcite concretions

Mineralogical composition observed with the microscope is largely confirmed by measurements of carbonate content and X-ray diffraction data (for X-ray diffractogram see appendix). Calcite concretions reach calcite contents of 85 wt.% on average and its host rock reaches calcite contents of ca. 84 wt.% (Table 2) as revealed by carbonate bomb analysis and supported by graphic evaluation of thin section images.

### 4.3.2 Siderite concretions

With the carbonate bomb carbonate contents of 70 wt.% on average were measured for siderite concretions as opposed to 34 wt.% for the host rock, a mudstone to claystone. Elemental analyzes of siderite concretions and the enclosing claystone from Wagreich et al. (2011) were used to calculate relative amounts of Fe, Mn, Mg and Ca (Table 3).

**Chemical composition of siderite concretions and their host rock (claystone)**

|  | Average concretion | | Average host rock | |
|---|---|---|---|---|
|  | wt% | mol% | wt% | mol% |
| $SiO_2$ (%) | 25.57 | | 58.75 | |
| $CO_2$ (%) | 22.26 | | 1.05 | |
| $SO_3$ (%) | 0.08 | | 0.20 | |
| FeO (%) | 28.11 | | 6.95 | |
| $FeCO_3$ (%) | 45.26 | 39.02 | 11.19 | 9.65 |
| MnO (%) | 0.99 | 1.40 | 0.04 | 0.06 |
| MgO (%) | 2.70 | 6.70 | 2.80 | 6.95 |
| CaO (%) | 7.40 | 13.21 | 0.85 | 1.52 |
| **Sum of mol%** | | **60.33** | | **18.17** |
| | | | | |
| rel. mol% Fe | | 63.92 | | 52.99 |
| rel. mol% Mn | | 2.27 | | 0.31 |
| rel. mol% Mg | | 11.35 | | 38.35 |
| rel. mol% Ca | | 22.45 | | 8.35 |
| **Sum of rel. mol%** | | **100.00** | | **100.00** |

Table 3: Selected elemental contents of siderite concretions and their host rock. Weight percent are taken from Wagreich et al. (2011), mol percent were calculated in this study.

## 4.4 Stable carbon and oxygen isotopes

$\delta^{13}C$ and $\delta^{18}O$ values of six calcite concretions, three siderite concretions, and their host rocks have been measured. Isotope data for the host rock of the siderite concretions were taken from Wagreich et al. (2011). To establish possible concentric trends, samples were taken along profiles from one calcite concretion, Fu1_12, its host rock, S1_12, and one siderite concretion, GAMS2_12 (Table 4). Fu1_12 shows variations of ~ 1‰ in $\delta^{13}C$ and $\delta^{18}O$ between the center and the margins. Both, $\delta^{13}C$ and $\delta^{18}O$ are slightly more negative in the center. The average over the entire profile of Fu1_12 ($\delta^{13}C$ = −6.3‰ and −8.4‰) fits well with the average values of the calcite concretions altogether ($\delta^{13}C$ = −5.8‰ and $\delta^{18}O$ = −8.4‰). The calcite concretion, which is most depleted in $^{13}C$ and $^{18}O$ is F3_12. It reveals a mean $\delta^{13}C$ value of −6.7‰ and a $\delta^{18}O$ value of −8.8‰. In contrast, F4_12 shows the highest $\delta^{13}C$ and $\delta^{18}O$ of all calcite concretions with $\delta^{13}C$ = −4.3‰ and $\delta^{18}O$ = −8.0‰ respectively. Their host rock appears just slightly enriched with $\delta^{13}C$ = −4.9‰ and $\delta^{18}O$ = −6.0‰ on average (Fig. 13).

| A: Calcite concretions | $\delta^{13}C$ | $\delta^{18}O$ |
| --- | --- | --- |
| Fu1_12_1 | −6.0 | −8.0 |
| Fu1_12_2 | −6.5 | −8.7 |
| Fu1_12_3 | −6.8 | −8.7 |
| Fu1_12_4 | −6.6 | −8.7 |
| Fu1_12_5 | −5.8 | −8.0 |
| **Fu1_12 (average; n=5)** | **−6.3** | **−8.4** |
| | | |
| F3_12_1 | −6.8 | −8.8 |
| F3_12_2 | −6.7 | −8.8 |
| **F3_12 (average; n=2)** | **−6.7** | **−8.8** |
| | | |
| F4_12_1 | −4.4 | −8.0 |
| F4_12_2 | −4.2 | −7.9 |
| **F4_12 (average; n=2)** | **−4.3** | **−8.0** |
| | | |
| G1_12_1 | −6.4 | −8.8 |
| G1_12_2 | −5.7 | −8.4 |
| **G1_12 (average; n=2)** | **−6.0** | **−8.6** |
| | | |
| G2_12_1 | −6.1 | −8.3 |
| G2_12_2 | −6.2 | −8.7 |
| **G2_12 (average; n=2)** | **−6.2** | **−8.5** |
| | | |
| G4_12_1 | −4.2 | −7.9 |
| G4_12_2 | −5.9 | −8.2 |
| **G4_12 (average; n=2)** | **−5.0** | **−8.1** |
| **Calcite concretions (average; n=15)** | **−5.8** | **−8.4** |

**B: Host rock calcites**

| | δ¹³C | δ¹⁸O |
|---|---|---|
| S1_12_1 | −5.5 | −6.1 |
| S1_12_2 | −4.2 | −5.8 |
| S1_12_3 | −5.3 | −6.0 |
| S1_12_4 | −4.8 | −6.1 |
| **Host rock calcite (average; n=4)** | **−4.9** | **−6.0** |

**C: Siderite concretions**

| | | |
|---|---|---|
| GAMS2-12-1 | −7.5 | −0.3 |
| GAMS2-12-2 | −10.1 | +1.8 |
| GAMS2-12-3 | −9.5 | +1.7 |
| GAMS2-12-4 | −10.4 | +1.8 |
| GAMS2-12-5 | −10.8 | +2.2 |
| GAMS2-12-6 | −9.9 | +1.6 |
| **GAMS2_12 (average; n=6)** | **−9.7** | **+1.5** |
| GAMS3-12-1 | −7.9 | +1.0 |
| GAMS3-12-2 | −8.7 | −3.5 |
| **GAMS3_12 (average; n=2)** | **−8.3** | **−1.2** |
| GAMS4-12-1 | −8.1 | +1.3 |
| GAMS4-12-2 | −11.1 | +0.9 |
| **GAMS4_12 (average; n=2)** | **−9.6** | **+1.1** |
| **Mean value siderite concretions** | **−9.2** | **+0.5** |

**D: Host rock siderites**

| | | |
|---|---|---|
| Host rock lower part (no concretions; average; n=6) | +0.4 | |
| Host rock middle part (concretions; average; n=15) | −1.7 | |
| Host rock upper part (concretions; average; n=10) | −0.1 | |
| **Host rock siderite (average; n=3)** | **−0.5** | |

Table 4: $\delta^{13}C$ and $\delta^{18}O$ values of calcite concretions (Fu1_12, F3_12, F4_12, G1_12, G2_12 and G4_12), host rock of calcite concretions (S1_12), siderite concretions (GAMS2_12, GAMS3_12 and GAMS4_12) and host rock of siderite concretions. Values are given in per mill (‰) relative to the V-PDB standard.

The siderite concretions exhibit a mean $\delta^{13}C$ value of −9.2‰ and a mean $\delta^{18}O$ value of +0.5%. Generally, they are internally more heterogeneous than the calcite concretions (Table 4). GAMS2_12, for example, has a relatively high $\delta^{13}C$ value of −7.5‰ along with a rather low $\delta^{13}C$ value of −10.8‰. $\delta^{18}O$ values of GAMS2_12 range from +2.2‰ to

−0.3‰. For both, $\delta^{13}$C and $\delta^{18}$O values, no obvious trend between the center and the margins is apparent, but it seems that $\delta^{13}$C and $\delta^{18}$O values are inversely correlated within this concretion. Within GAMS3_12 and GAMS4_12, $\delta^{13}$C and $\delta^{18}$O values are directly correlated. The lowest $\delta^{13}$C has been measured in GAMS4_12 (−11.1‰), the highest $\delta^{13}$C in GAMS2_12 (−7.5‰), the lowest $\delta^{18}$O in GAMS3_12 (−3.5‰) and the highest $\delta^{18}$O in GAMS2_12 (+2.2‰) (Table 4 and Fig. 13). According to Wagreich et al. (2011) $\delta^{13}$C values of the host rock range from −8.9‰ to +1.2‰ and $\delta^{18}$O values from −5.5‰ to −1.0‰ and comprise therefore more positive $^{13}$C and more negative $^{18}$O signatures than the siderite concretions. Due to lack of more detailed data, these values could not be incorporated in Table 4 and Fig. 13. The authors present additional data for different sections of the host rock. The lower part, which does not contain concretions (pers. comm. M. Wagreich) has a $\delta^{13}$C value of +0.4‰, the middle and the upper part (both concretion-bearing) a $\delta^{13}$C value of −1.7‰ and −0.1‰ respectively. The calculated average of these three values is −0.5‰. Wagreich et al. (2011) do not mention the corresponding $\delta^{18}$O values.
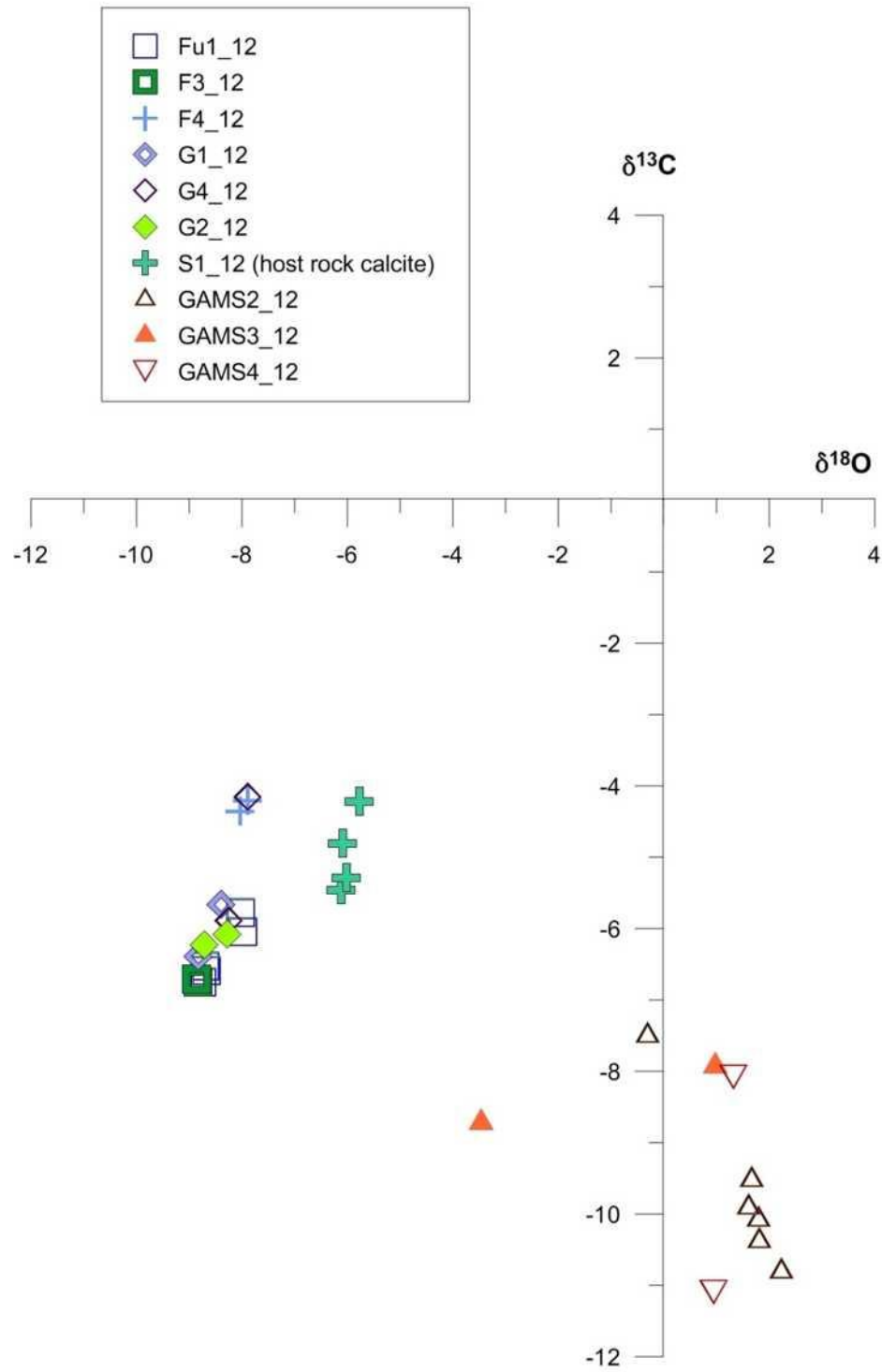
Fig. 10: Crossplot of $\delta^{18}O$ against $\delta^{13}C$ values of all calcite concretions and their host rock and all siderite concretions. Values are given in per mill with respect to the V-PDB standard.

## 4.5 Lipid biomarker inventory

### 4.5.1 Hydrocarbons

The hydrocarbon fractions of all concretions prior and after decalcification predominantly contain *n*- alkanes with chain lengths from 15 to 35 carbon atoms only in the siderite extract after decalcification chain lengths up to 37 carbon atoms are found (Table 5). Hydrocarbons of calcite concretion F4_12 prior decalcification reveal an asymmetrical, bimodal distribution, the two bulges maximize at $n$-$C_{19}$ and $n$-$C_{31}$ (Fig. 14). After decalcification, the contents in the hydrocarbon fraction of F4_12 decreased by ca. 50% (Table 6). Concretion G4_12 has a unimodal hydrocarbon distribution peaking at $n$-$C_{31}$ (Fig. 15). Higher contents for hydrocarbons are found after decalcification. The siderite concretion GAMS4_14, contains only minor amounts of hydrocarbons (Table 6). The most abundant compound of GAMS4_12 prior decalcification is $n$-$C_{18}$, the least abundant component is $n$-$C_{32}$. *n*-alkanes are uniformly distributed prior and after decalcification (Fig.16). It has to be noted that GAMS4_12 after decalcification reveals hydrocarbons with higher carbon numbers, up to $n$-$C_{37}$. Fig. 17 gives an overview of long-chain *n*-alkanes before and after decalcification. Apart from *n*-alkanes, the isoprenoid hydrocarbons pristane (2,6,10,14-tetramethylpentadecane) and phytane (2,6,10,14-tetramethylhexadecane) are present in F4_12 (Table 5), representing 1% of total hydrocarbons and being slightly less abundant in the decalcified fraction. Nevertheless, the contents are most likely lower, since they are coeluting with cycloalkanes. Pentacylic triterpenoids are represented by 11 hopanes occurring in the hydrocarbon fraction from $C_{27}$ (trisnorhopane) to $C_{31}$ (homohopane) (Table 5). Hopanes elute between the *n*-alkanes $n$-$C_{28}$ to $n$-$C_{35}$. A detailed view of hopanes in the different samples is given in Fig. 18. Hopanes of F4_12 make up 4% of the undecalcified and 4.2% of the decalcified fractions. In G4_12 they represent 4% before and after decalcification. Siderite concretion GAMS4_12 reveals hopanes only prior decalcification (2%). After decalcification, hopanoids are absent. Among hopanes of F4_12, $\beta\beta$ trisnorhopane is the most abundant, and $\alpha\beta$ homohopane the least abundant in fractions prior and after decalcification. Other than saturated hopanes, the monounsaturated hop-17(21)-ene is identified and interestingly more abundant after decalcification in samples F4_12 as well as in G4_12. $\beta\beta$ Norhopane is the second most abundant hopanoid in both calcite concretions, but less abundant after decalcification. In G4_12 again $\beta\beta$ trisnorhopane is the most abundant hopane, prior and after decalcification. $\beta\beta$ Hopane and $\beta\beta$ homohopane are absent in the decalcified part. As the trivial names of hopanoids are used here, IUPAC names plus

chemical formulas and molecular weights are displayed in the appendix.

| Hydrocarbons | F4_12 | | G4_12 | | GAMS4_14 | |
|---|---|---|---|---|---|---|
| Compound | undiss. | diss. | undiss. | diss. | undiss. | diss. |
| n-$C_{14:0}$ | n.d. | n.d. | n.d. | n.d. | n.d. | n.d. |
| n-$C_{15:0}$ | 0.11% | 0.39% | 0.20% | n.d. | n.d. | n.d. |
| n-$C_{16:0}$ | 0.78% | 1.29% | 0.64% | n.d. | 4.09% | n.d. |
| n-$C_{17:0}$ | 2.60% | 2.34% | 1.35% | n.d. | 9.23% | n.d. |
| Pristane + Cycloalkane* | 1.64% | 0.95% | n.d. | n.d. | n.d. | n.d. |
| n-$C_{18:0}$ | 5.17% | 4.13% | 2.29% | n.d. | 11.61% | 0.15% |
| Phytane + Cycloalkane** | 1.54% | 1.30% | n.d. | n.d. | n.d. | n.d. |
| n-$C_{19:0}$ | 6.22% | 4.87% | 2.85% | 1.11% | 10.45% | 0.20% |
| n-$C_{20:0}$ | 4.83% | 3.61% | 2.45% | 1.51% | 10.08% | 0.26% |
| n-$C_{21:0}$ | 2.93% | 2.36% | 2.12% | 1.99% | 7.78% | 0.29% |
| n-$C_{22:0}$ | 2.09% | 2.01% | 1.87% | 2.19% | 6.62% | 0.35% |
| n-$C_{23:0}$ | 3.58% | 3.77% | 3.81% | 4.31% | 6.06% | 0.76% |
| n-$C_{24:0}$ | 2.46% | 2.44% | 2.15% | 3.12% | 5.45% | 2.02% |
| n-$C_{25:0}$ | 5.43% | 5.16% | 5.58% | 6.76% | 5.45% | 4.91% |
| n-$C_{26:0}$ | 2.92% | 2.84% | 2.83% | 3.76% | 3.13% | 8.33% |
| n-$C_{27:0}$ | 7.47% | 8.14% | 8.28% | 9.11% | 3.24% | 8.69% |
| n-$C_{28:0}$ | 3.55% | 3.60% | 3.36% | 4.31% | 3.78% | 8.17% |
| Trisnorhopene | 0.32% | 0.14% | n.d. | 0.73% | n.d. | n.d. |
| n-$C_{29:0}$ | 13.52% | 14.86% | 17.30% | 17.38% | 4.33% | 6.54% |
| $\beta\beta$ Trisnorhopane | 1.02% | 0.76% | 1.02% | 0.73% | n.d. | n.d. |
| n-$C_{30:0}$ | 2.82% | 3.37% | 4.28% | 3.92% | 1.58% | 13.62% |
| $\alpha\beta$ Norhopane | 0.19% | 0.35% | 0.07% | 0.35% | 0.55% | n.d. |
| Hop-17(21)-ene | 0.53% | 0.56% | 0.26% | 0.60% | n.d. | n.d. |
| $\beta\alpha$ Normoretane | 0.13% | 0.23% | 0.33% | 0.49% | n.d. | n.d. |
| n-$C_{31:0}$ | 15.71% | 17.75% | 21.18% | 21.96% | 3.10% | 7.44% |
| $\alpha\beta$ Hopane | 0.34% | 0.21% | 0.36% | 0.42% | 0.57% | n.d. |
| $\beta\beta$ Norhopane | 0.98% | 0.77% | 0.84% | 0.35% | 0.30% | n.d. |
| n-$C_{32:0}$ | 1.84% | 1.48% | 2.11% | 2.59% | 0.63% | 6.46% |
| $\alpha\beta$ Homohopane | 0.11% | 0.17% | 0.14% | 0.50% | 0.28% | n.d. |
| $\beta\alpha$ Homomoretane | 0.33% | 0.35% | 0.44% | 0.61% | 0.59% | n.d. |
| $\beta\beta$ Hopane | 0.29% | 0.42% | 0.32% | n.d. | n.d. | n.d. |
| n-$C_{33:0}$ | 6.48% | 7.34% | 8.42% | 9.22% | 1.02% | 7.52% |
| n-$C_{34:0}$ | 0.53% | 0.54% | 1.31% | 0.80% | n.d. | 7.21% |
| $\beta\beta$ Homohopane | 0.35% | 0.29% | 0.24% | n.d. | 0.09% | n.d. |
| n-$C_{35:0}$ | 1.20% | 1.21% | 1.63% | 1.91% | n.d. | 6.60% |
| n-$C_{36:0}$ | n.d. | n.d. | n.d. | n.d. | n.d. | 6.60% |
| n-$C_{37:0}$ | n.d. | n.d. | n.d. | n.d. | n.d. | 3.90% |

Table 5: Relative percentages of hydrocarbons; undiss. = lipids before decalcification; diss. = lipids after decalcification; n.d. = not detected; *potentially 1,5-dimethylheptylbenzene;**potentially 1,5-dimethyloctylbenzene or 1,5,9-trimethylnonylbenzene.

Fig. 11: A: Partial gas chromatogram (total ion current) of the hydrocarbon fraction of F4_12 before decalcification. Circles: *n*-alkanes; stars: hopanes; Pri: pristane; Phy: phytane; Std.: standard, 5α-cholestane; B: Partial chromatogram (total ion current) of the hydrocarbon fraction of F4_12 before decalcification, from *n*-$C_{27}$ to *n*-$C_{35}$. Circles: *n*-alkanes; stars: hopanes; purple: designation of hopanes.

| | Total amount of lipids [µg/g sediment] | | |
|---|---|---|---|
| Samples | F1 - Hydrocarbons | F3 - Alcohols | F4 - Fatty acids |
| F4_12 undissolved | 0.37 | 0.16 | 0.73 |
| F4_12 dissolved | 0.17 | 0.08 | 1.84 |
| G4_12 undissolved | 0.77 | 0.87 | 6.00 |
| G4_12 dissolved | 1.35 | 1.61 | 21.75 |
| GAMS4_12 undissolved | 0.10 | 0.16 | 1.61 |
| GAMS4_12 dissolved | 0.35 | 0.02 | 2.23 |

Table 6: Contents of lipids of all samples analyzed.



Fig. 12: Partial gas chromatogram (total ion current) of the hydrocarbon fraction of G4_12 after decalcification. Circles: *n*-alkanes; cont.: contaminant; Std.: standard, 5α-cholestane.
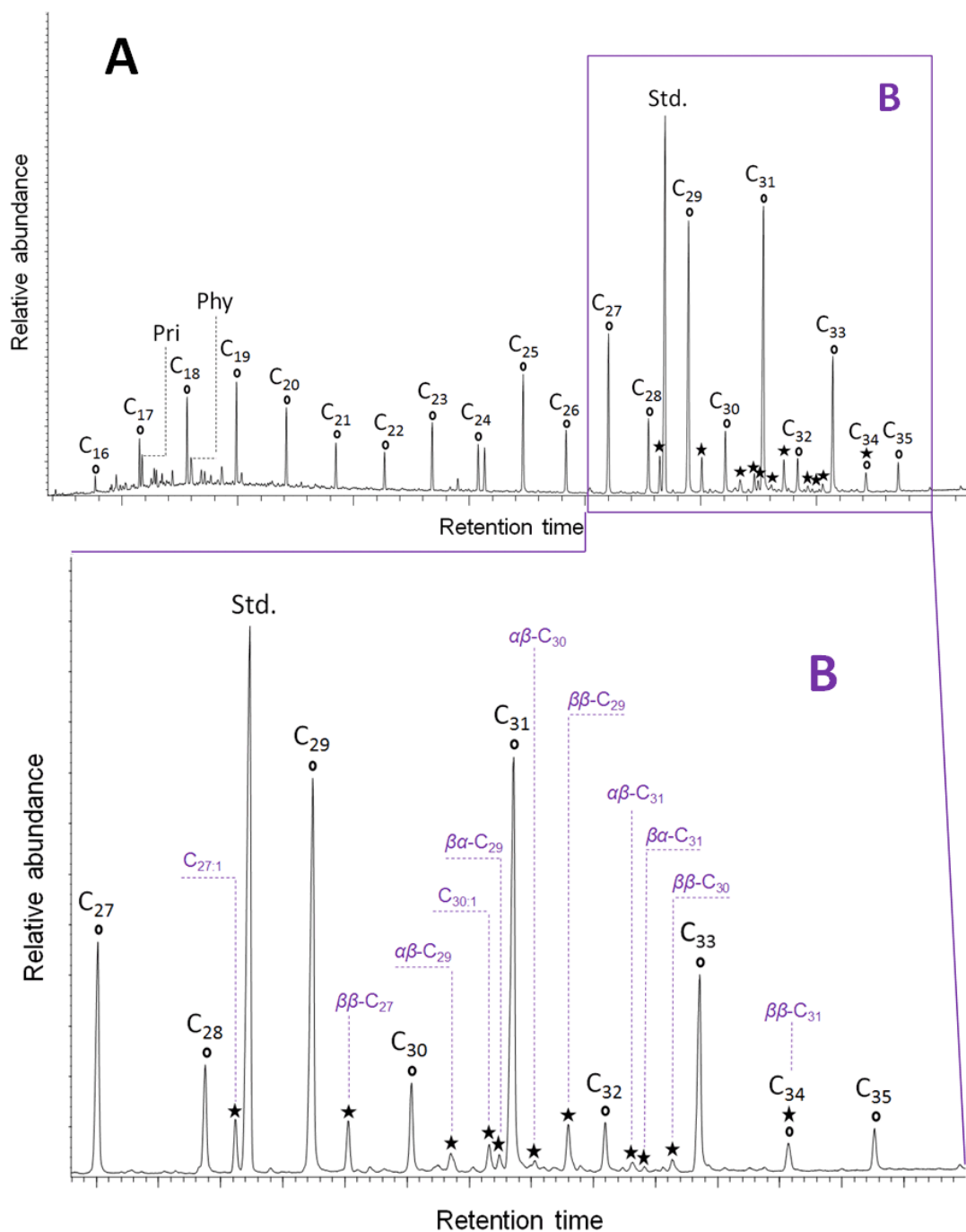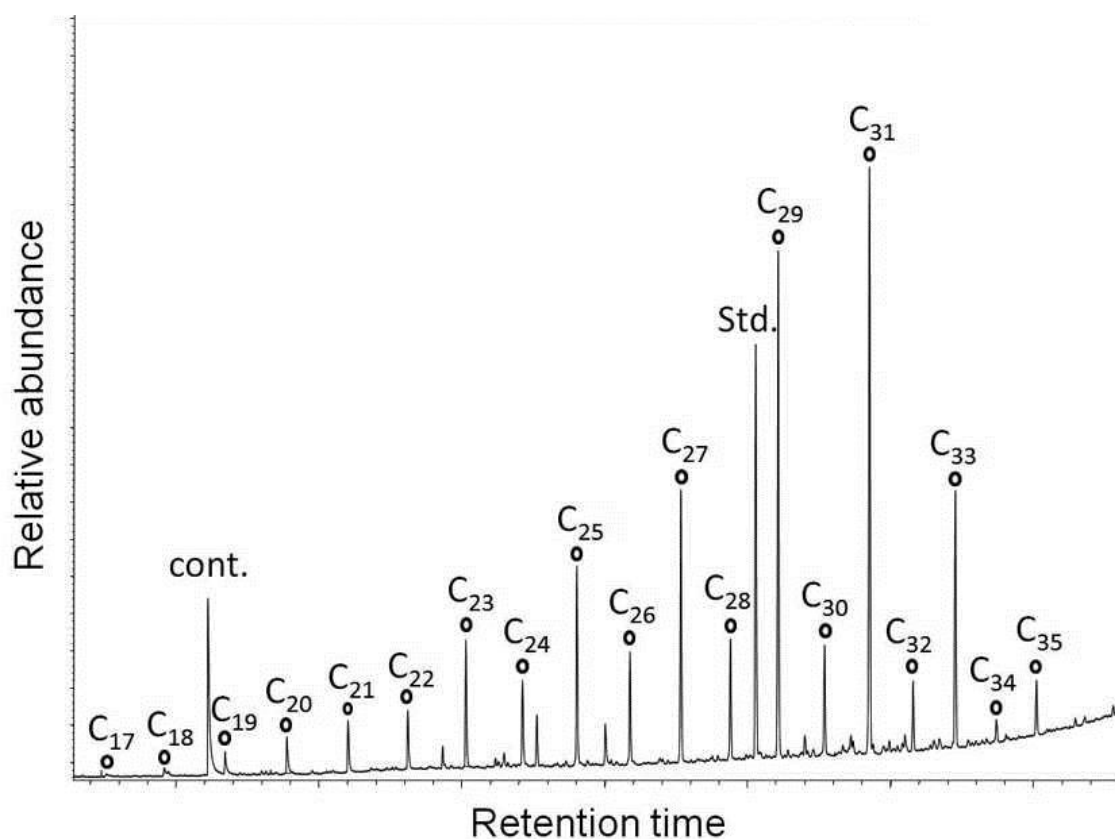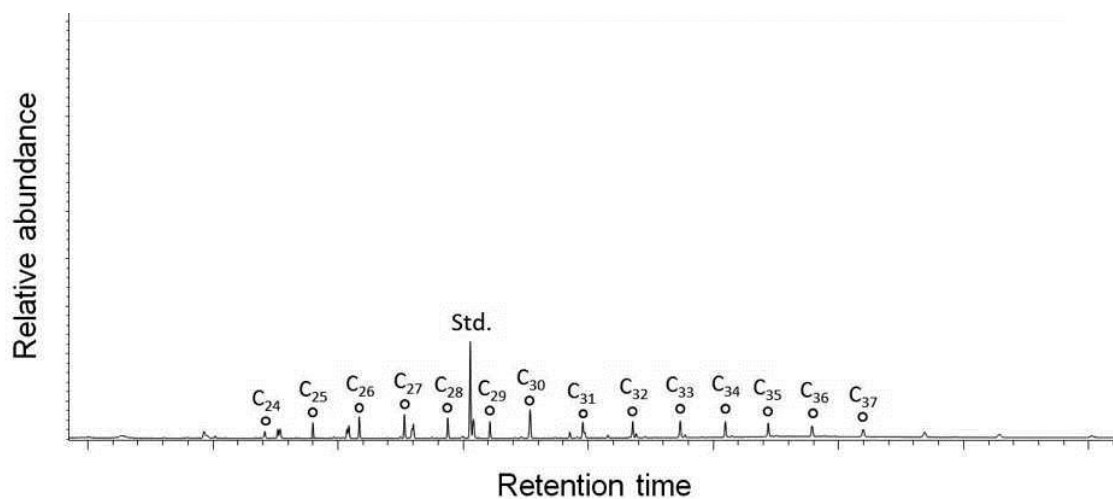
Fig. 13: Partial gas chromatogram (total ion current) of the hydrocarbon fraction of GAMS4_12 after decalcification. Circles: *n*-alkanes; Std.: standard, 5α-cholestane.
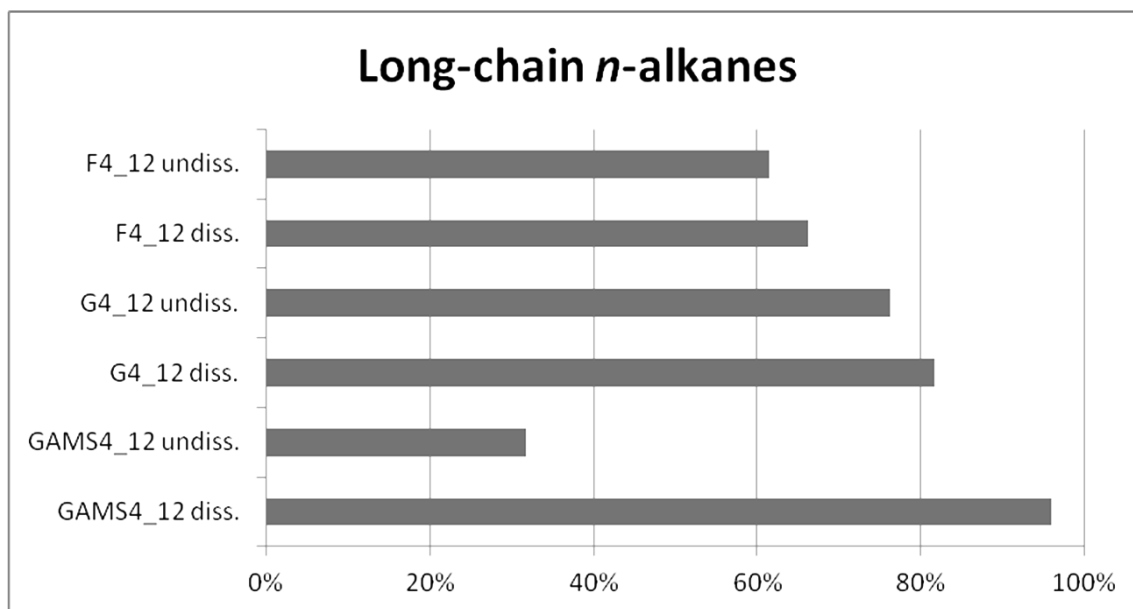


Fig. 14: Relative percentages of long-chain *n*-alkanes (of all hydrocarbons detected) in all samples. "undiss." = undecalcified; "diss." = decalcified.
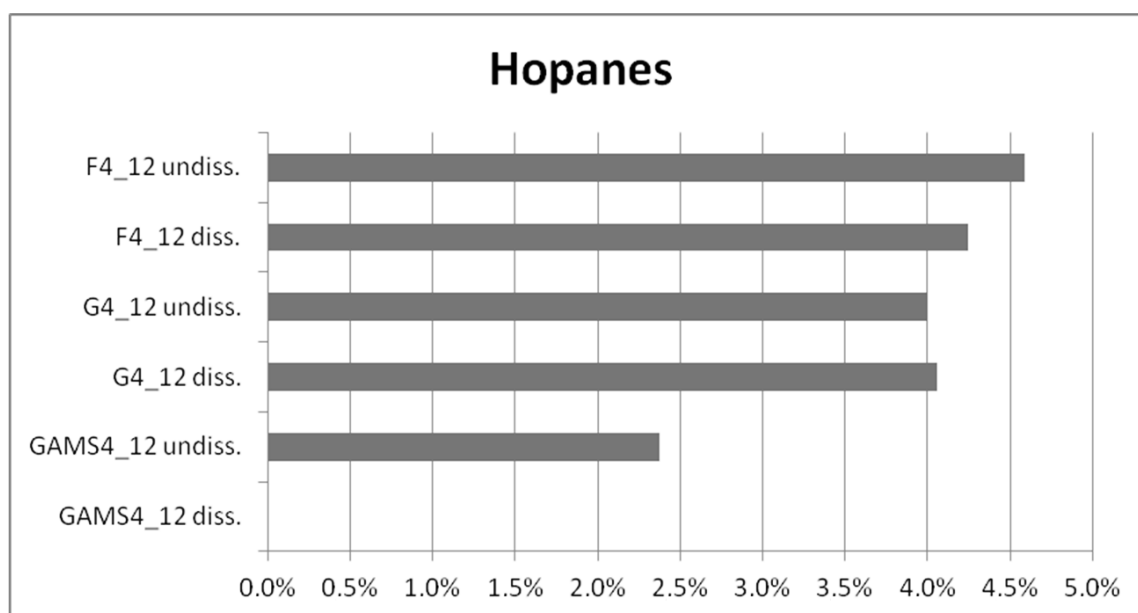
Fig. 15: Relative percentages of hopanes (of all hydrocarbons detected) in all samples. "undiss." = undecalcified; "diss." = decalcified.

For further characterization of *n*-alkanes, three parameters describing the length distribution of *n*-alkanes were calculated (cf., Kiriakoulakis et al., 2000; El-Shafeiy et al., 2014). The carbon preference index (CPI) describes the freshness of long-chain *n*-alkanes and *n*-alkanoic acids by comparing the amounts of odd- and even-numbered carbon chains (El-Shafeiy et al., 2014 and references therein). Land plants produce leaf waxes composed of long-chain *n*-alkanes ($C_{25}$-$C_{35}$) predominated by odd-numbered carbon chains (Eglinton et al., 1962). For long-chain alcohols and fatty acids, even-numbered chains are predominating (Eglinton et al., 1962; Gaines et al., 2009, p. 9-15). During diagenesis the original land plant signature is modified, which can be determined by calculating the CPI. For hydrocarbons the odd-numbered *n*-alkanes $C_{25}$ and $C_{27}$ are divided over the even-numbered *n*-alkanes $C_{26}$ and $C_{28}$. For alcohols and fatty acids it is vice versa, even-numbered *n*-alcohols or *n*-fatty acids are divided over odd-numbered, *n*-alcohols or *n*-fatty acids. The CPI was calculated for alkanes and fatty acids. The long-chain *n*-alkanes in the calcite concretions (F4_12 and G4_12) indicate moderate maturation according to the CPI with values around 2 (Table 7). Generally, a distinct odd-over-even predominance can be still observed. The variation in the CPI between the undecalcifed and the decalcified results are only minor (Table). In contrast, the siderite concretion shows a CPI around 1.

The ratio of short- to long-chain hydrocarbons is expressed as LMW/HMW (Low Molecular Weight/High Molecular Weight). Most authors, such as Kiriakoulakis et al. (2000), Gao et al. (2007) and Wang et al. (2007) define LMW alkanes as *n*-alkanes up to 20 carbons, and HMW those with 21 carbons or more. In this study, the cut-off is placed between $C_{24}$ and $C_{25}$, because this better accords with the findings of Eglinton et al. (1962), about how leaf waxes are constituted. The LMW/HMW in F4_12 is almost

similar prior and after decalcification (Table 7). In both cases, the HMW alkanes dominate over LMW alkanes by a factor 2. In concretion G4_12, LMW alkanes comprise an even smaller part of alkanes with an LMW/HMW of 0.25 and 0.17 for undecalcifed and decalcified, respectively. Siderite concretion GAMS4_14 shows a very different pattern. The sample prior decalcification contains a three times higher abundance of LMW alkanes than HMW alkanes. In contrast, the decalcified fraction is almost barren of LMW alkanes (LMW/HMW = 0.04). Fig. 17 compares the relative amounts of long-chain $n$-alkanes ($> C_{24}$) of all hydrocarbons measured. Long-chain $n$-alkanes make up a major part of total hydrocarbons, with higher percentages prior decalcification, most significantly in the siderite concretion.

The Terrestrial-Aquatic Ratio (TAR) is used by Bourbonniere & Meyers (1996) and El-Shafeiy et al. (2014) in their study to determine the terrestrial portion of their hydrocarbons. They define it as the ratio between the sum of $n$-$C_{27}$, $n$-$C_{29}$ and $n$-$C_{31}$ and the sum of $n$-$C_{15}$, $n$-$C_{17}$ and $n$-$C_{19}$. The long-chain components represent terrestrial sources and the short-chain components aquatic sources. It must be taken into account that land-derived organic matter primarily contains higher proportions of $n$-alkanes than aquatic algae do. The $n$-alkanes derived from algae are mainly degradation products of fatty acids. Accordingly, especially in fresh samples the TAR may be biased and may overrepresent terrestrial input (Bourbonniere & Meyers, 1996). Due to an incomplete occurrence of components in the samples it was not always possible to calculate this ratio. In such cases this is expressed in Table 7 as "n.c." for "not calculated". The TAR of the calcite concretions seems to be rather high. F4_12 has a TAR around 4 of the undecalcified and a TAR of more than 5 of the decalcified part. In G4_12 the value is even higher (11) for the undecalcified part, whereas the decalcified part could not be calculated. For the siderite concretion GAMS4_12, only the TAR for the undecalcified fraction is available with a comparably low value of 0.5.

| Hydrocarbons | F4_12 | | G4_12 | | GAMS4_14 | |
| --- | --- | --- | --- | --- | --- | --- |
| | undiss. | diss. | undiss. | diss. | undiss. | diss. |
| CPI | 1.99 | 2.06 | 2.24 | 1.97 | 1.26 | 0.82 |
| LMW/HMW | 0.50 | 0.41 | 0.26 | 0.17 | 2.71 | 0.04 |
| TAR | 4.11 | 5.36 | 10.64 | n.c. | 0.54 | n.c. |

Table 7: Selected parameters of alkane distributions; CPI = $(C_{25}+C_{27})/(C_{26}+C_{28})$; LMW/HMW: sum of $n$-alkanes $\leq C_{24}$ divided over sum of $n$-alkanes $\geq C_{25}$; TAR = $(C_{27}+C_{29}+C_{31})/(C_{15}+C_{17}+C_{19})$. "undiss." = undecalcified; "diss." = decalcified.

## 4.5.2 Alcohols

The alcohol fraction did not contain any meaningful components and will not be described here.

### 4.5.3 Carboxylic acids

The carboxylic acid or fatty acid fraction is dominated by *n*-fatty acids, but also contains branched fatty acids and hopanoic acids of minor abundance. The majority of carboxylic acids are saturated (Table 8). Nevertheless, various unsaturated carboxylic acids occur, such as $C_{15:1}$, $C_{16:1}$, $C_{17:1}$, $C_{18:1}$, $C_{18:2}$, $C_{22:1}$ and $C_{24:1}$ fatty acids and hopenoic acids. Further, short-chain, methyl-branched, saturated fatty acids occur in low amounts. Straight-chain fatty acids range from $C_{12}$ to $C_{33}$, revealing a rather uniform distribution, except for the two most prominent peaks, $C_{16}$ and $C_{18}$. $C_{18}$ (41–59% on average) is more abundant than $C_{16}$ (24–34% on average) (Fig. 19). This pattern occurred in all samples analyzed.

| Fatty acids | F4_12 | | G4_12 | | GAMS4_12 | |
|---|---|---|---|---|---|---|
| | undiss. | diss. | undiss. | diss. | undiss. | diss. |
| *n*-$C_{12:0}$ | n.d. | n.d. | n.d. | 0.95% | 0.36% | n.d. |
| *n*-$C_{13:0}$ | n.d. | n.d. | n.d. | 0.09% | n.d. | n.d. |
| *iso*-$C_{14:0}$ | n.d. | n.d. | n.d. | 0.17% | n.d. | n.d. |
| *n*-$C_{14:0}$ | 1.30% | 0.86% | 1.00% | 2.31% | 3.17% | 0.96% |
| *iso*-$C_{15:0}$ | 0.08% | 0.23% | 0.07% | 0.46% | 0.21% | 0.04% |
| *anteiso*-$C_{15:0}$ | 0.11% | 0.34% | 0.11% | 0.29% | 0.40% | 0.06% |
| *n*-$C_{15:0}$ | 0.35% | 0.40% | 0.33% | 0.70% | 0.97% | 0.28% |
| *iso*-$C_{16:0}$ | 0.09% | 0.30% | 0.09% | 0.16% | n.d. | 0.07% |
| $C_{15:1}$ | 0.52% | n.d. | n.d. | n.d. | 0.16% | n.d. |
| $C_{16:1}$ | n.d. | 0.28% | 0.23% | n.d. | n.d. | n.d. |
| $C_{16:1}$ | n.d. | 0.72% | 0.21% | 0.31% | 3.51% | 0.37% |
| *n*-$C_{16:0}$ | 26.56% | 24.31% | 27.68% | 27.80% | 33.86% | 30.82% |
| 10Me-$C_{16:0}$ | n.d. | n.d. | n.d. | traces | n.d. | n.d. |
| Unknown branched $C_{16:0}$ | n.d. | n.d. | n.d. | 0.05% | n.d. | 0.08% |
| *iso*-$C_{17:0}$ | 0.11% | 0.20% | 0.12% | 0.32% | 0.34% | 0.16% |
| *anteiso*-$C_{17:0}$ | 0.21% | 0.33% | 0.20% | 0.22% | 0.17% | 0.30% |
| $C_{16:1}$ | 0.10% | n.d. | n.d. | n.d. | n.d. | n.d. |
| $C_{17:1}$ | n.d. | 0.40% | n.d. | n.d. | 0.25% | n.d. |
| *n*-$C_{17:0}$ | 0.66% | 0.82% | 0.66% | 0.76% | 0.63% | 0.69% |
| $C_{18:2}$ | n.d. | n.d. | 0.18% | 0.24% | 1.70% | 0.29% |
| $C_{18:1}$ | 2.45% | 3.12% | 1.70% | 0.91% | 5.96% | 2.86% |
| $C_{18:1}$ | n.d. | n.d. | 0.26% | 0.22% | n.d. | 0.47% |
| *n*-$C_{18:0}$ | 47.90% | 47.80% | 48.26% | 41.40% | 43.86% | 59.03% |
| *n*-$C_{19:0}$ | n.d. | 0.42% | 0.38% | 0.42% | 0.17% | 0.19% |
| *n*-$C_{20:0}$ | 1.29% | 1.73% | 1.64% | 1.65% | 1.04% | 1.47% |
| *n*-$C_{21:0}$ | 0.42% | 0.77% | 1.04% | 1.14% | 1.97% | n.d. |
| *n*-$C_{22:0}$ | 1.18% | 1.57% | 1.68% | 2.11% | 0.41% | 0.39% |
| *n*-$C_{23:0}$ | 1.18% | 1.29% | 1.08% | 1.70% | 0.17% | n.d. |
| *n*-$C_{24:0}$ | 1.76% | 1.91% | 1.09% | 2.41% | 0.37% | 0.39% |

| | | | | | | |
|---|---|---|---|---|---|---|
| $n$-$C_{25:0}$ | 1.24% | 0.94% | 0.70% | 1.27% | n.d. | n.d. |
| $n$-$C_{26:0}$ | 1.86% | 1.45% | 0.98% | 1.91% | 0.19% | 0.21% |
| $n$-$C_{27:0}$ | 1.05% | 0.59% | 0.80% | 0.90% | n.d. | 0.11% |
| $C_{22:1}$ | n.d. | n.d. | 0.41% | n.d. | n.d. | n.d. |
| $n$-$C_{28:0}$ | 2.61% | 1.52% | 1.59% | 2.27% | 0.12% | 0.24% |
| $n$-$C_{29:0}$ | n.d. | 0.36% | 0.63% | 0.72% | n.d. | 0.10% |
| $C_{24:1}$ | n.d. | n.d. | 0.26% | n.d. | n.d. | n.d. |
| $n$-$C_{30:0}$ | 2.31% | 1.04% | 1.82% | 1.89% | n.d. | 0.18% |
| $\alpha\beta$ Hopenoic acid | n.d. | n.d. | 0.14% | n.d. | n.d. | n.d. |
| $n$-$C_{31:0}$ | n.d. | 0.17% | 0.44% | 0.40% | n.d. | n.d. |
| $\alpha\beta$ Hopanoic acid | n.d. | n.d. | 0.05% | n.d. | n.d. | n.d. |
| $\beta\beta$ Homohopenoic acid | n.d. | n.d. | 0.11% | n.d. | n.d. | n.d. |
| $n$-$C_{32:0}$ | 1.81% | 0.46% | 1.23% | 1.04% | n.d. | 0.22% |
| $\beta\alpha$ Hopanoic acid | n.d. | n.d. | 0.03% | n.d. | n.d. | n.d. |
| $n$-$C_{33:0}$ | n.d. | n.d. | 0.23% | n.d. | n.d. | n.d. |
| $\alpha\beta$ Homohopanoic acid | n.d. | 0.16% | 0.03% | 0.17% | n.d. | n.d. |
| $\beta\beta$ Hopanoic acid | 0.12% | 0.13% | 0.06% | 0.14% | n.d. | n.d. |
| $\beta\alpha$ Homohopanoic acid | n.d. | n.d. | 0.05% | n.d. | n.d. | n.d. |
| $n$-$C_{34:0}$ | n.d. | n.d. | n.d. | n.d. | n.d. | n.d. |
| $\beta\beta$ Bishomohopenoic acid | n.d. | 0.21% | 0.07% | n.d. | n.d. | n.d. |
| $\alpha\beta$ Bishomohopanoic acid | n.d. | 0.28% | 0.50% | 0.37% | n.d. | n.d. |
| $\beta\beta$ Homohopanoic acid | 0.81% | 0.96% | 0.51% | 0.33% | n.d. | n.d. |
| $n$-$C_{35:0}$ | n.d. | n.d. | n.d. | n.d. | n.d. | n.d. |
| $\beta\beta$ Bishomohopanoic acid | 1.52% | 3.11% | 1.10% | 1.17% | n.d. | n.d. |
| $\alpha\beta$ Trishomohopanoic acid | 0.11% | 0.15% | 0.05% | 0.04% | n.d. | n.d. |
| $\beta\beta$ Trishomohopanoic acid | 0.29% | 0.55% | 0.17% | 0.31% | n.d. | n.d. |
| $\beta\beta$ Tetrakishomohopanoic acid | n.d. | 0.13% | n.d. | n.d. | n.d. | n.d. |

Table 8: Relative percentages of carboxylic acids; undiss. = lipids before decalcification; diss. = lipids after decalcification; n.d. = not detected.
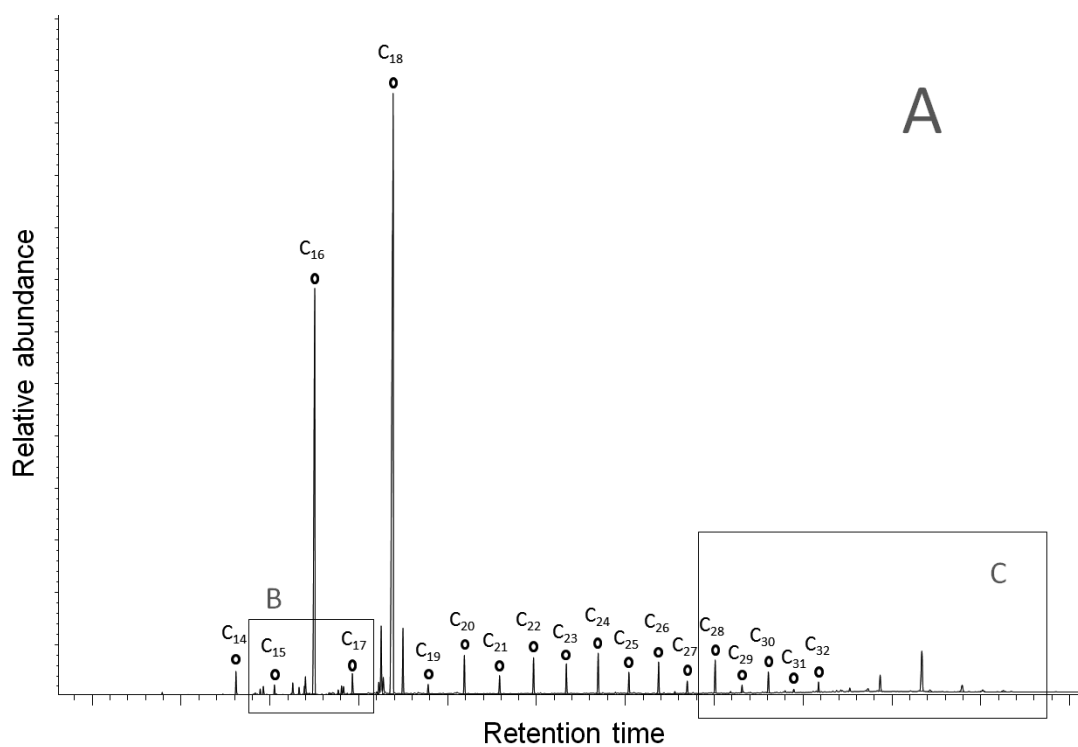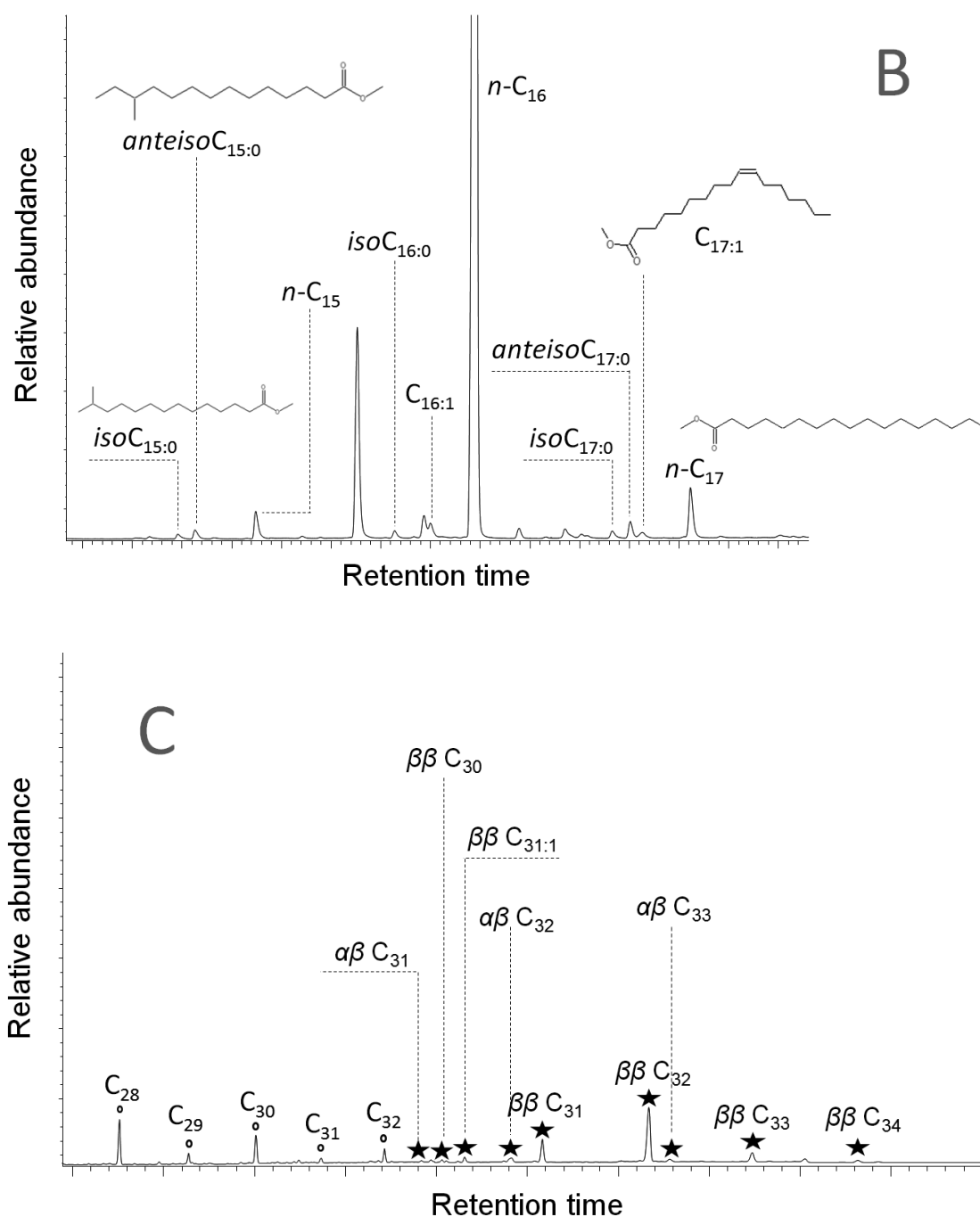
Fig. 16: A: Partial gas chromatogram (total ion current) of the fatty acid fraction of F4_12 after decalcification (measured as fatty acid methyl esters). Circles: *n*-fatty acids. B: Close-up of the gas chromatogram of the fatty acid fraction of F4_12 after decalcfication (measured as fatty acid methyl esters), showing short-chain, branched and unsaturated fatty acids. C: Close-up of the gas chromatogram of the fatty acid fraction of F4_12 after decalcification (measured as fatty acid methyl esters), showing hopanoic acids.

The short-chain, branched fatty acids comprise *iso*-$C_{14:0}$, *iso*-$C_{15:0}$, *anteiso*-$C_{15:0}$, *iso*-$C_{16:0}$, 10Me-$C_{16:0}$, branched $C_{16:0}$, *iso*-$C_{17:0}$ and *anteiso*-$C_{17:0}$. *Iso*-$C_{14:0}$ and 10Me-$C_{16:0}$ occur just in the decalcified G4_12, the former with 0.17% and the latter just in traces. The "branched $C_{16:0}$" could not be identified due to low contents. Fig. 20 gives an overview of

the percentages of total short-chain branched fatty acids relative to the total carboxylic acid fraction inventory. Branched fatty acids make up 0.6% (undecalcified) and 1.4% (decalcified) in F4_12, 0.6% (undecalcified) and 1.6% (decalcified) in G4_12, and 1.1% (undecalcified) and 0.6% (decalcified) in GAMS4_12. Generally, the contents of short-chain branched fatty acids are slightly increased after decalcification. In contrast, the siderite concretion shows the opposite trend. The *anteiso*-$C_{15:0}$ and -$C_{17:0}$ are more abundant than the equivalent *iso* fatty acid, in all fractions except G4_12 after decalcification and GAMS4_12 before decalcification (the latter just for *iso* and *anteiso*-$C_{17:0}$). The most abundant short-chain branched fatty acids are *iso*-$C_{15:0}$ and *anteiso*-$C_{15:0}$ (0.23–0.46%) in the decalcified fractions of F4_12 and G4_12 and the undecalcified fraction of GAMS4_12, *iso*-$C_{16:0}$ (0.30%) in the decalcified F4_12 and *iso*-$C_{17:0}$ and *anteiso*-$C_{17:0}$.
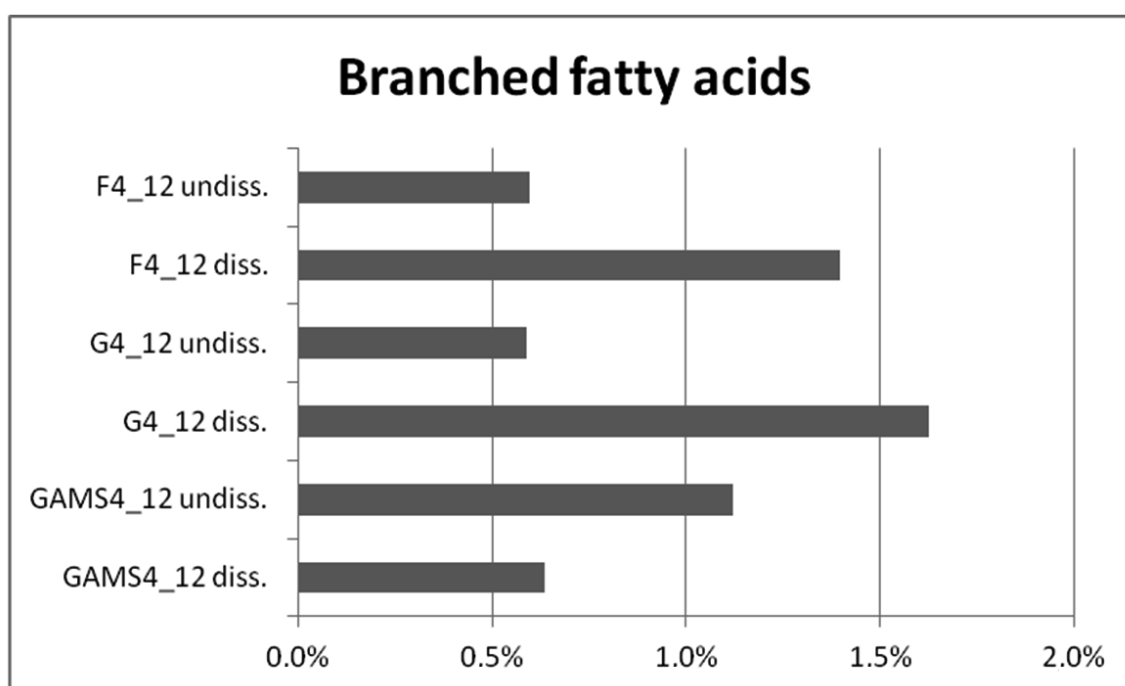


Fig. 17: Relative percentages of branched fatty acis (of all carboxylic acids detected) in all samples. "undiss." = undecalcified; "diss." = decalcified.

Apart from fatty acids, various hopanoic acids were identified in the carboxylic acid fractions (Table 8). They range from *αβ* hopenoic acid, eluting after *n*-$C_{30:0}$ to *ββ* tetrakishomohopanoic acid, eluting after *n*-$C_{35:0.}$ As shown in Fig. 21, hopanoic acids are increasing in F4_12 from undecalcified (2.9%) to decalcified (5.8%) and are decreasing in G4_12 (2.9% to 2.5%). The most abundant hopanoids in F4_12 and G4_12 are *ββ* homohopanoic acid and *ββ* bishomohopanoic acid (Fig. 19B). Least abundant hopanoids are *αβ* hopanoic acid, *βα* hopanoic (moretanoic) acid and *βα* homohopanoic (homomoretanoic) acid. For more details see Table 8. No hopanoic acids were detected in the siderite concretion. Overall, *ββ* isomers predominate over *αβ* isomers. The *ββ* configuration is the original, biological isomer (biohopanoids) and the *αβ* and *βα* isomers are the geological equivalents (geohopanoids) (e.g., Farrimond et al., 2002). As for the

hopanoids of the hydrocarbon fractions, the full information on compounds are listed in the appendix.
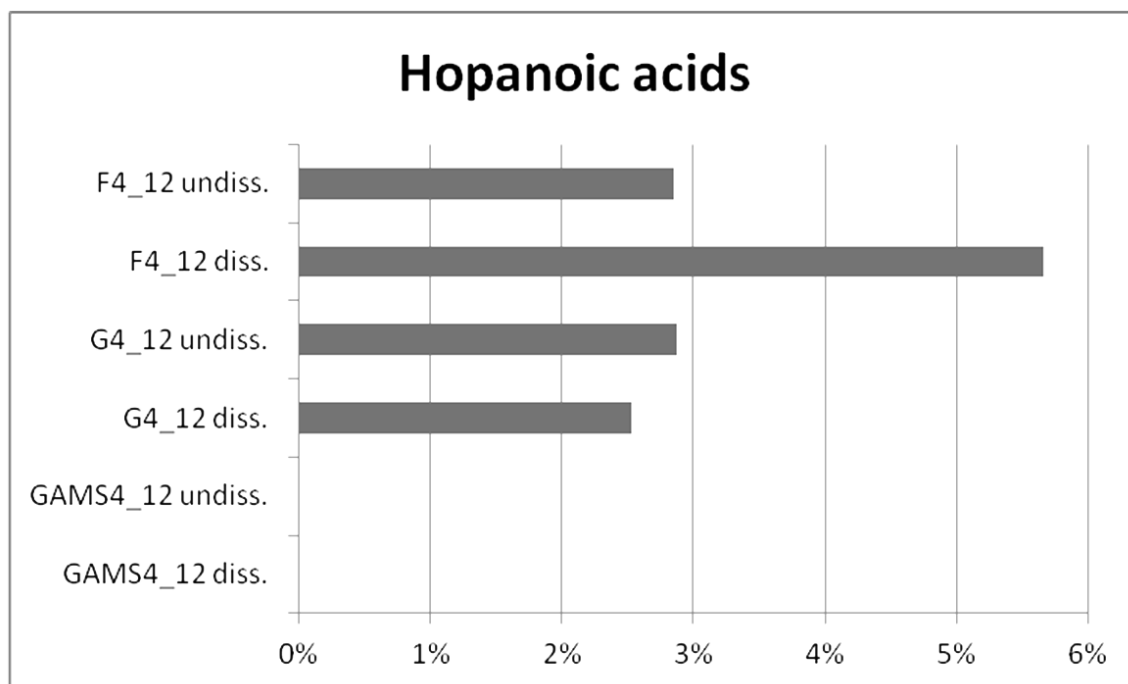


Fig. 18: Relative percentages of hopanoic acids (of all carboxylic acids detected) in all samples.

CPI of fatty acids were calculated by dividing even-numbered straight-chain fatty acids $C_{26}$ and $C_{28}$ over odd-numbered $C_{25}$ and $C_{27}$. CPIs of calcite concretions are very similar to the hydrocarbon fractions with values of moderate maturity from 1.7 to 2.0 (Table 9). No remarkable difference was observed between the samples before and after decalcification. For the siderite concretion the CPIs could not be calculated due to the lacking of some of the compounds.

The LMW/HMW was calculated in the same way as for hydrocarbons by dividing amounts of short-chain fatty acids up to $C_{24}$ over long-chain fatty acids above $C_{25}$. F4_12 and G4_12 show an opposite trend in LMW/HMW (Table 9). LMW/HMW is higher after decalcification for F4_12 (8 vs. 12) and it is the other way round for G4_12 (10 vs. 8). Extremely high LMW/HMW were calculated for GAMS4_12, namely 288 undissolved and 89 dissolved.

TAR of the fatty acids were calculated by dividing ($C_{24}$+$C_{26}$+$C_{28}$) over ($C_{12}$+$C_{14}$+$C_{16}$). Again, the first sum represents terrestrial material and the second sum marine organic matter. Generally, TAR of fatty acids are lower than those of the hydrocarbons. TAR of calcite concretions are in the range of 0.1 to 0.2 and TAR of the siderite concretion are even lower, showing values in the order of 0.01 (Table 9).

| Fatty acids | F4_12 | | G4_12 | | GAMS4_14 | |
|---|---|---|---|---|---|---|
| | undiss. | diss. | undiss. | diss. | undiss. | diss. |
| CPI | 1.95 | 1.95 | 1.71 | 1.93 | n.c. | n.c. |
| LMW/HMW | 7.53 | 12.42 | 10.07 | 7.80 | 288.30 | 88.88 |
| TAR | 0.22 | 0.19 | 0.13 | 0.21 | 0.02 | 0.03 |

Table 9: Selected parameters of fatty acid distributions; CPI = $(C_{26}+C_{28})/(C_{25}+C_{27})$; LMW/HMW: sum of $n$-fatty acids $\leq C_{24}$ divided over sum of n-fatty acids $\geq C_{25}$; TAR = $(C_{24}+C_{26}+C_{28})/(C_{12}+C_{14}+C_{16})$.

# 5 Interpretation

## 5.1 Concentric vs. pervasive growth

Combined results of microscopic, geochemical and isotopic observations were applied to study the growth geometry of the concretions. The siderite concretions do not have septarian fractures, show bioturbation, but no decrease in cement content toward the margin and no isotopic trend in the measured profiles. Further, the siderite concretions consist of two different cements throughout their entire bodies; (i) siderite microspar and (ii) subsequent, pore-filling ferroan calcite. Mozley (1996) as well as Raiswell & Fisher (2000) interpret this as evidence for pervasive growth and together with the other observations it seems very probable that the siderite concretions of Gams indeed grew pervasively.

Raiswell & Fisher (2000) state that it is generally more difficult to suggest a growth mode for calcite concretions, since the results are less clear than for siderite concretions. In this work, no textural or geochemical trend from center to margin was found, indicating pervasive growth (Mozley, 1996; Raiswell & Fisher, 2000). Further, no increase of siliciclastics (proven by analysis of carbonate content) and no clear isotopic trend were observed. However, the applied methods possibly could not distinguish between authigenic and detrital calcite. The observed bioturbation is, according to Raiswell & Fisher (2000), an evidence that concretion formation already began close to the sediment-water interface. The authors justify this statement with the argument that the preservation of burrows requires a certain resistance against compaction and concurrent plasticity, which allows the burrows to be formed. They further argue that remaining plasticity is just possible, if the mode of growth is pervasive. The presence of septarian cracks also requires a concretion, which reached its final volume, but is still in a plastic state (Hounslow, 1997; Pratt, 2001). Mozley (1996) moreover considered that very porous sediments would not be able to support a fully cemented, dense concretion, and suggested the presence of a low-density organic soap as an intermediate state. The geometry of growth cannot be ascertained for the calcite concretions, but pervasive growth seems more likely than concentric growth.

## 5.2 Septaria

The calcite concretions of Steinbrunn contain significant septarian cracks. Septarian cracks are very common in concretions (Astin, 1986; Pratt, 2001). To date, various explanations exist for septaria formation in the literature. Astin (1986) suggested that these fractures are the result of tensile stress caused by overpressure applied on the concretion and its host, Duck (1995) interpreted them as subaqueaous shrinkage cracks generated by the conversion of a calcium "soap" of fatty acids to calcite, Sellés-Martínez (1996) suggested amplification of stress around a stiff concretion in a more plastic sediment, and Hounslow (1997) developed a model similar to that of Astin (1986) with the difference that the pressure has to be higher inside the concretion than in the surroundings (higher pore pressure due to permability loss by cementation of the concretion). Other theories are chemical desiccation of a colloid, gas expansion (gas produced by the decay of organic matter) or synaresis of a gel-like intermediate state of the interior (Sellés-Martínez, 1996; Pratt, 2001; Pearson et al., 2005). Pratt (2001) presented a rather innovative idea by explaining septarians as a result of earthquake-induced ground motion, applied on concretions with stiff exteriors, while the interiors are still soft. A statement of Astin (1986) and Hounslow (1997) could be important for this study, namely that, if septarian cracks show an orientation in horizontal sections, this may be an indicator for anisotropic stress by tectonics or for directional anisotropy in the growth rates. As the region experienced tectonic deformation (Grundtner et al., 2009 and references therein), tectonic stress appears to be a feasible explanation for the septarian cracks. However, also an anisotropic growth may be possible, as the cracks are oriented parallel to the elongation in F4_12 (Fig. 6C). Wieninger et al. (2009) suggest a combination of the models of Astin (1986), Hounslow (1997) and Pratt (2001) for the calcite concretions of Steinbrunn. The samples of this study have not been taken orientated and there are not sufficient horizontal sections of them. Therefore, an unequivocal assignment of an exact formation mechanism of the septarian cracks cannot be made.

## 5.3 Precipitation of carbonate cements

### 5.3.1 The effects of microbial oxidation of organic matter

It is widely accepted that carbonate concretions may be products of microbial metabolism in the sedimentary column (e.g. Irwin et al., 1977, for further references see introduction). Briefly, here it will be shown how iron reduction, sulfate reduction and methanogenesis can induce carbonate precipitation. Loyd et al. (2012a) provided a detailed review of these processes among others:

Iron reduction

$$(CH_2O)_{106}(NH_3)_{16}H_3PO_4 + 424Fe(OH)_{3\,(s)} + 742CO_2 + 13.5H^+ \rightarrow 15NH_4^+ + 0.5HPO_4^{2-}$$
$$+ \, 0.5H_2PO_4^- + 848HCO_3^- + 424Fe^{2+} + 318H_2O \tag{1}$$

Sulfate reduction

$$(CH_2O)_{106}(NH_3)_{16}H_3PO_4 + 53SO_4^{2-} + 13.5H^+ \rightarrow 15NH_4^+ + 0.5HPO_4^{2-} + 0.5H_2PO_4^-$$
$$+ \, 53CO_2 + 53HCO_3^- + 53HS^- + 53H_2O \tag{2}$$

Methanogenesis

$$2HCO_3^- + 4H_2 \rightarrow CH_4 + CO_3^{2-} + 3H_2O \tag{3}$$
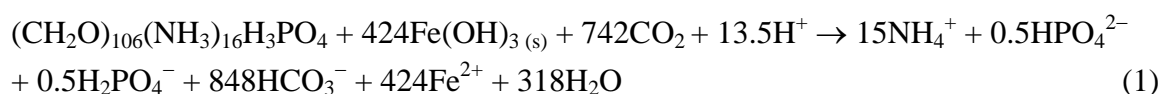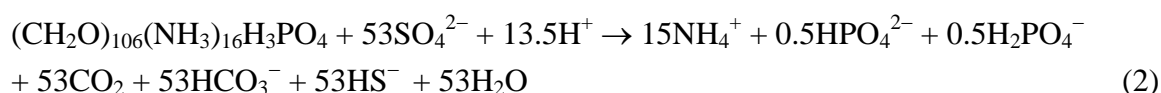
Where applicable, reactions involving organic carbon are written in accordance with the Redfield Ratio. Iron reduction (eq. 1) consumes a large quantity of protons and produces bicarbonate. Sulfate reduction (eq. 2) generates carbon dioxide and decreases therefore the pH, but it also generates bicarbonate, which rises carbonate alkalinity. Autotrophic methanogenesis (eq. 3) does not produce bicarbonate, but it increases the pH. Both factors, bicarbonate production and pH increase can contribute to the formation of carbonate minerals (eq. 4 from Coleman, 1985; eq. 5 modified after Coleman, 1985):

Precipitation of calcite

$$Ca^{2+} + HCO_3^- + OH^- \rightarrow CaCO_3 + H_2O \tag{4}$$

Precipitation of siderite

$$Fe^{2+} + HCO_3^- + OH^- \rightarrow FeCO_3 + H_2O \tag{5}$$

The acidity generated by sulfate reduction is commonly consumed by biogenic or abiogenic reduction of ferric iron. Ferric iron can be reduced abiogenically with the sulfide produced by bacterial sulfate reduction. Sulfide has a very high affinity to iron and if both are present in the system, iron monosulfides and pyrite will precipitate (eq. 6 and 7 from Loyd et al. 2012a):

Pyrite formation

$$5H^+ + 2Fe(OH)_{3\ (s)} + HS^- \rightarrow 2Fe^{2+} + S° + 6H_2O \hspace{3cm} (6)$$

$$Fe^{2+} + HS^- + S°_{(s)} \rightarrow FeS_{2\ (s)} + H^+ \hspace{4cm} (7)$$

Although the precipitation reaction (eq. 7) releases protons, this effect is compensated by the reduction of iron (eq. 1 and 6), which is necessary for pyrite formation. In conclusion, the prerequisite for carbonate precipitation through sulfate reduction is the presence of suffic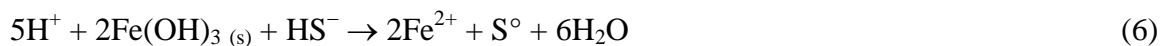ient iron, for which pyrite can be an indicator. Authors such as Coleman & Raiswell (1995) and Wilkin & Barnes (1997) further state that the precipitation of framboidal pyrite, as observed in the thin sections (see petrography), need not, but can be induced by bacterial sulfate reduction.


### 5.3.2 Stable carbon and oxygen isotopes – evidence of an organic matter origin of bicarbonate?

If the bacterial oxidation of organic matter or autotrophic methanogenesis were involved in the precipitation of carbonate, this is commonly reflected in the stable carbon isotopy of the carbonate minerals (Irwin et al., 1977; Coleman, 1985; Siegel et al., 1987; Pye et al., 1990; Coleman et al., 1993; Kiriakoulakis et al., 2000; Raiswell & Fisher, 2004; Reitner et al., 2005; Natalicchio et al., 2014). Iron- or sulfate- reducing bacteria are most often assimilating carbon heterotrophically in such environments. As a consequence, the generated carbon dioxide or dissolved bicarbonate is not fractionated significantly and has the same $\delta^{13}C$ value as the source from which it derived (Irwin et al., 1977). Marine organic matter has $\delta^{13}C$ values between −30‰ and −20‰ (Irwin et al., 1977; Coleman, 1985; Siegel et al., 1987; Pye et al., 1990; Coleman et al., 1993; Kiriakoulakis et al., 2000; Pratt, 2001; Raiswell & Fisher, 2004; Pearson & Nelson, 2005; Ziegenbalg et al., 2010; 2012; Mortimer et al., 2011; Loyd et al., 2014). Nevertheless the $\delta^{13}C$ values of the carbonate carbon is less depleted, because not only organic matter is the source, but also marine dissolved inorganic carbon, which has a $\delta^{13}C$ value around 0‰. Consequently, the $\delta^{13}C$ values of diagenetic carbonate precipitated in a marine environment in the zone of iron reduction or sulfate reduction lies somewhere between −30‰ and 0‰, depending on the mixing of the two carbon sources (Irwin et al., 1977; Coleman, 1985; 1993; Pye et al., 1990; Peckmann et al., 1999; Raiswell & Fisher, 2004; Loyd et al., 2012a; 2012b). In contrast, autotrophic, methanogenic archaea are highly selective in terms of their carbon source. Biogenic methane is very depleted in heavy carbon (−110‰ to −50‰ $\delta^{13}C$), while the residual carbon dioxide becomes enriched in $^{13}C$ (+15‰). Carbonate minerals precipitated in the zone of methanogenesis have therefore positive $\delta^{13}C$ values (Irwin et al., 1977; Siegel et al., 1987; Kiriakoulakis et al., 2000; Lash and Blood, 2004; Raiswell & Fisher, 2004; Pearson & Nelson, 2005; Ziegenbalg et al., 2010; Hoffmann-Sell et al., 2011; Birgel et al., 2015).

The calcite concretions have $\delta^{13}C$ values of −5.8‰ on average. This can be explained by a mixture of incorporation of organic carbon from iron- or sulfate reduction and marine dissolved inorganic carbon for carbonate formation. However, the host sediments are considered to be rather brackish or even limnic. Nevertheless, the thin sections with the very abundant corallinacean red algae proof that bioclastic, marine limestone ("Leithakalk") from the Badenian, formed a substantial part of the detritus. It seems plausible that the adjacent elevated area of the Leithagebirge delivered sufficient material. This model is also consistent with the somewhat higher $\delta^{13}C$ value (−4.9‰) of the host sediment. The portion of organogenetic carbonate is therefore a little lower than in the concretion body.

The oxygen isotopes of carbonate minerals are a function of the parent fluid composition and the temperature of precipitation, if one value is known, the second can be calculated (Irwin et al., 1977; Mortimer & Coleman, 1997; Kiriakoulakis et al., 2000; Raiswell & Fisher, 2000; Lash & Blood, 2004; Pearson & Nelson, 2005; Loyd et al., 2014). Mortimer & Coleman (1997), Kiriakoulakis et al. (2000), Raiswell & Fisher (2000) and Antler et al. (2013) additionally emphasize the role of biological fractionation of oxygen isotopes. Mortimer & Coleman (1997) state that iron-reducing bacteria preferentially take up $^{16}O$, which induces the precipitation of $^{18}O$ depleted siderite, and Antler et al. (2013) compare the enrichment in heavy oxygen and sulfur isotopes of the residual sulfate pool during sulfate reduction. Antler et al. (2013) further assume if a lot of organic matter is available and sulfate reduction rates are high, then the $\delta^{18}O$ of the residual sulfate increases more slowly in relation to the $\delta^{34}S$ at the same time, assuming that sulfate reduction rates were low. Indeed, the biological effects of iron reduction and sulfate reduction are unexpectedly high and in the range of other factors lowering the $\delta^{18}O$ of carbonates, such as higher temperature of precipitation or recrystallization, influx of meteoric water or precipitation of other, $^{18}O$ enriched, minerals (Irwin et al, 1977; Pye et al., 1990; Mozley & Wersin, 1992; Mortimer & Coleman, 1997; Raiswell & Fisher, 2000; Pearson & Nelson, 2005; Antler et al., 2013; Loyd et al., 2014). Overall the $\delta^{18}O$ values of the calcite concretions (−8.4‰) and the host sediment (−6.0‰) could reflect either the effect of microbial fractionation, a mixing with meteoric waters, the (re)crystallization at higher temperatures or a combination of all mechanisms. The $\delta^{18}O$ waters of meteoric waters can range from near seawater composition to extremely low values (−20‰ by Mozley & Wersin, 1992 and −80‰ by Raiswell & Fisher, 2000). The fact that the concretions reveal a $\delta^{18}O$ value somewhat lower than the surrounding sediment could be attributed to the activity of organic matter-degrading bacteria.

The mean $\delta^{13}C$ value of the siderite concretions (−9.2‰) is more negative than the calcite concretions. Therefore, a slightly higher contribution of organic matter derived carbon or a more $^{13}C$ depleted organic matter can be assumed. According to Wagreich et al. (2011) carbonate of the siderite host rock show high, marine $\delta^{13}C$ and depleted $\delta^{18}O$ values,

relative to the concretion bodies. It seems that $^{18}O$ depleted, maybe warm and/or meteoric waters could have circulated more easily through the surrounding sediment than through the less permeable concretions themselves. The marine $\delta^{13}C$ values in comparison with the rather negative $\delta^{13}C$ values of the concretions confirms the model that organic matter oxidation was restricted to the site, where the concretions formed.

Most likely siderite formation took place either in the iron reduction or the sulfate reduction zone. However, as siderite precipitated, the sulfate reduction zone can be excluded, because ferrous iron has a higher affinity for sulfide than for carbonate (e.g. Coleman, 1985). As long as sulfide is present it will outcompete carbonate in the struggle for iron. Only if all sulfide is used up and iron is still available, the precipitating carbonates can be ferroan calcite, ferroan dolomite, ankerite or siderite (Coleman, 1985; Pye et al., 1990; Coleman et al., 1993; Coleman & Raiswell, 1995; Duan et al., 1996; Mortimer et al., 2011). In most natural systems, too less iron is available and the most common assemblage is iron-free calcite with pyrite (Coleman, 1985; Coleman & Raiswell, 1995). Hence, the precipitation of siderite concretions requires a system with very low seawater sulfate. This is the reason why many diagenetic siderites were thought to be formed in freshwater environments by methanogenesis (Coleman et al., 1993). However, this option can be excluded for the siderites of the current study for several reasons. First, as mentioned above, autotrophic methanogenesis would produce a characteristic, positive $\delta^{13}C$ signature in the concretion. Second, the siderites are clearly of marine origin, as revealed by the geological background (Wagreich et al., 2011). Nevertheless, the elemental results must be taken with caution, since the siderite concretions not only contain authigenic siderite, but also authigenic calcite and detrital minerals, which all contribute to the bulk rock data presented here. However, also carbon (−9.2‰) and oxygen (+0.5‰) isotopes are typical for marine siderite, according to Mozley & Wersin (1992), who analyzed a wide range of marine and continental siderites. Coleman (1985), Pye et al. (1990), Coleman et al. (1993), Duan et al. (1996) and Mortimer et al. (2011) present an alternative model for the generation of diagenetic siderite in marine sediments. They suggest that siderite can precipitate in restricted areas of biotic iron reduction, which do not receive any contribution of sulfide from the sulfate reduction zone. As soon as sulfide (most often as hydrogen sulfide) enters this zone, it leads to the dissolution of siderite and the formation of pyrite (Coleman, 1985). Mortimer et al. (2011) developed a model, where coupled biotic and abiotic iron reduction produces elemental sulfur and siderite in a recent salt marsh (north Norfolk coast, UK). In their scenario, high sedimentation rates preserve reactive, ferric iron in depth, while seawater sulfate becomes relatively diluted in a way that iron reduction exceeds sulfate reduction at the site of concretion formation. They also state that in salt marshes, reactive iron contents are typically higher than in other marine sediments. The host sediment of the concretions of Gams does not comprise salt marsh sediments, but according to Wagreich et al. (2011) the sedimentation rates were very high, which could have promoted FeR, dilution of sulfate and subsequent precipitation of siderite.

### 5.3.3 Lipid biomarkers in concretions - do they leave behind signatures of microbes participating in mineral formation?

One further possibility to test if microbial activity was involved in the formation of diagenetic minerals and which metabolism was active is the extraction and analysis of lipid biomarkers preserved in the mineral matrix. The major difficulty arising is to distinguish between authentic, primary signals and secondary inputs and/or contamination. To exclude secondary signatures and contaminations, a special procedure was applied. It is described already in the material and methods section, but the most important point is that for each sample lipid biomarkers were extracted twice; prior and after decalcification. The first extract contains compounds, which are most likely representing secondary contributions. The compounds of the second extraction, as trapped within the carbonate crystal lattice, are assumed to have been directly involved into the precipitation of the carbonates and can be considered at least as pristine biomarkers.

The isoprenoids pristane and phytane, for example, which occur only in the calcite concretion F4_12, are less abundant after decalcification. Among others, Rontani & Bonin (2011) reviewed the sources of isoprenoid hydrocarbons in the marine environment. They mention chlorophyll, tocopherols (or vitamin E) from cyanobacteria, micro- and macroalgae and higher plants; and archaeal lipids (archaeols) as possible sources. In this study, no archaeal lipids have been found, neither in F4_12, nor in any other sample. And as it additionally seems that pristane and phytane are secondary here, it can be excluded that they derive from archaea. In contrast, there is abundant evidence for a significant input of terrestrial plant detritus, as described below. Hence, it is more likely that pristane and phytane derive either from chlorophyll or tocopherols of higher land plants.

However, also within the extract after decalcification, there are constituents, which cannot be related to the processes that led to concretion formation. The calcite concretions were formed in a basin, which was characterized by separation from the Paratethys and continuing inflow of freshwater. The freshwater obviously transported terrigenous material into this increasingly brackish pond, demonstrated by the abundant, plant wax-derived long-chain *n*-alkanes in the hydrocarbon fractions of the calcite concretions. Long-chain *n*-alkanes and *n*-fatty acids mainly originate from leaf waxes covering and protecting the leaves, stems, flowers and pollen of higher land plants, as supposed by authors such as Eglinton et al. (1962), Pearson et al. (2005), Rommerskirchen et al. (2006), Gaines et al. (2009), Heindel et al. (2012), Knoll et al. (2012), Guido et al. (2013) and Thiel et al. (2014). The fact that these land plant markers are particularly abundant in the extract after decalcification shows that these compounds were buried already in the sediments, where the concretions subsequently grew. The sedimentary organic matter is consequently incorporated into the calcite crystals and represents the conditions in the water column and possibly also hinterland. The moderate maturity of the hydrocarbons is

in good agreement with this hypothesis. The almost equal maturity of the carboxylic acids confirms that hydrocarbons and carboxylic acids of the calcite concretions were incorporated at more or less the same time and are thus also intrinsic to the carbonate. Nevertheless, while the hydrocarbons are of mainly terrestrial origin, carboxylic acids have a significantly higher proportion of short chains and thus a predominantly aquatic source (see Bourbonniere & Meyers, 1996 and Pearson et al., 2005 for further information about short-chain *n*-alkanes and *n*-fatty acids).

Palmitic ($n$-$C_{16:0}$) and stearic ($n$-$C_{18:0}$) acid are the most abundant components in all fatty acid fractions. The high proportions of these fatty acids seem rather typical for ancient carbonate concretions as has been demonstrated by Kiriakoulakis et al. (2000) and Pearson et al. (2005) for their Jurassic concretions, but it is widely accepted that palmitic and stearic acid are ubiquitous in eukaryotes and bacteria, and therefore are very unspecific (pers. comm. D. Birgel). In contrast, unsaturated fatty acids of low carbon numbers can be specific for certain groups of bacteria (Table 10). However, double bonds are highly unstable and the unsaturated fatty acids of this study have been treated as secondary and not significant.

Short-chain branched fatty acids are specific for various bacterial sources, are not produced by eukaryotes (Table 10), and they are more resistant than unsaturated fatty acids. Among the most reliable branched fatty acids is 10Me-$C_{16:0}$, which is a biomarker for the sulfate-reducing bacterial genus *Desulfobacter* (e.g. Coleman et al., 1993), which, however, occurs only in traces. Whereas *iso*-$C_{15:0}$ and *anteiso*-$C_{15:0}$, *iso*-$C_{16:0}$ and *iso*-$C_{17:0}$ and *anteiso*-$C_{17:0}$ are present in minor, but still significant amounts among fatty acids of the calcite concretions. They are present especially in the extracts after decalcification. Moreover, the general predominance of *anteiso*- over *iso*- fatty acids in our samples is in accord with findings by Rütters et al. (2001), who analyzed pure cultures of sulfate-reducing bacteria. These authors found a predominance of *anteiso*-fatty acids in the lipids of *Desulfosarcina variabilis*. Birgel et al. (2011) detected a similar pattern in lipids extracted from microbially-derived methane seep carbonates from the environment, where *Desulfosarcina/Desulfococcus* species live in a consortium with methane-oxidizing archaea. Possibly, *Desulfosarcina* or other sulfate-reducing bacteria may have been the producers of *iso*- and *anteiso*-fatty acids.

**Short-chain branched and unsaturated fatty acids and glycerolethers**

| Compound | Organsims | References |
|---|---|---|
| *iso*- and *anteiso*-$C_{15:0}$ and –$C_{17:0}$ | many bacteria, incl. SRB (*Desulfovibrio* sp., *Geobacter* sp., *Desulfosarcina* sp. and *Desulforhabdus* sp.) | Coleman et al., 1993; Rütters et al., 2001; Heindel et al., 2012; Guido et al., 2013; Thiel et al., 2014 |
| $iC_{16:0}$, $iC_{18:0}$, $iC_{19:0}$ and $aiC_{19:0}$ | unspecified bacteria | Guido et al., 2013 |
| $10Me$-$C_{16:0}$ | *Desulfobacter* sp. | Coleman et al., 1993; Duan et al., 1996; Kiriakoulakis et al., 2000; Elvert et al., 2003; Pearson et al., 2005; Heindel et al., 2012; Ziegenbalg et al., 2012; Guido et al., 2013 |
| $C_{16:1\omega5c}$ | *Desulfosarcina/Desulfococcus, Desulfotalea, Desulfobulbus, Desulforhabdus* and *Desulforhopalus* sp. | Rütters et al., 2001; Elvert et al., 2003 |
| $C_{16:1\omega7c}$ | *Geobacter* sp. and *Shewanella* sp. | Coleman et al., 1993 |
| $iC_{17:1\omega7c}$ | *Desulfovibrio* sp., *Desulfosarcina* sp. | Coleman et al., 1993; Duan et al., 1996; Kiriakoulakis et al., 2000; Rütters et al., 2001; Pearson et al., 2005; Heindel et al., 2012; Ziegenbalg et al., 2012; Guido et al., 2013 |
| $C_{17:1\omega6c}$ | *Desulfobulbus, Desulforhabdus* and *Desulforhopalus* sp. | Duan et al., 1996; Elvert et al., 2003 |
| MAGEs (monoalkyl glycerolethers) | few bacteria, incl. SRB | Heindel et al., 2012; Ziegenbalg et al., 2012; Guido et al., 2013 |
| DAGEs (dialkyl glycerolethers) | unspecified marine bacteria and SRB | Ziegenbalg et al., 2012; Guido et al., 2013 |

Table 10: Short-chain branched and unsaturated fatty acids and glycerolether, which may serve as biomarkers for different strains of sulfate-reducing bacteria (SRB).

Apart from aliphatic compounds, hopanoids are present in appreciable amounts. Hopanoids are biomarkers of bacteria. Although many bacteria have the theoretical ability to synthesize them, just around 10% of bacteria effectively do this (Rohmer et al., 1984; Pearson et al., 2007). Hopanoids were originally suggested to act as cell membrane rigidifiers, but in recent years other functions have been suggested as well, but were not finally proven until now (see Blumenberg et al., 2006; Eickhoff et al., 2013 and references therein). They have traditionally been assumed to be restricted to bacteria thriving in oxic environments. Nevertheless, Blumenberg et al. (2006) and Eickhoff et al. (2013) among others showed that also strictly anaerobic bacteria can produce hopanoids. Both studies detected diploptene (hop-22(29)-ene) among other hopanoids in pure cultures of sulfate-reducing bacteria of the genus *Desulfovibrio* and iron-reducing bacteria of the genus *Geobacter*. Diploptene was not the most abundant hopanoid in these studies, but it is particularly interesting for the current work as its geological degradation product hop-17(21)-ene was found in the hydrocarbon extract after decalcification and hence assumed to be pristine. Geohopanoids derive either from bacteriohopanepolyols (BHPs, 35 carbons and four or more functional groups; see Talbot & Farrimond, 2007) or from $C_{30}$ hopanoids such as diploptene or diplopterol (Farrimond et al., 2002; for further information see appendix).

Trisnorhopanes and norhopanes are the most abundant hopanoids in the hydrocarbon fractions of the calcite concretions. However, as these compounds lost up to three groups from the $C_{30}$ basic hopanoid backbone, they have lost any specificity. Also $\beta\beta$ bishomohopanoic acid, the dominant hopanoid in the carboxylic acid fraction, cannot be assigned to a specific precursor. Farrimond et al. (2002) describe the $\beta\beta$ $C_{32}$ hopanoic acid as a substantial part of the lipid biomarker inventory of modern sediments. Also in this work, the primary, biological isomer ($\beta\beta$) is more abundant than the secondary, geological isomer ($\alpha\beta$), which was observed as a general trend of all hopanoic acids and is used as evidence of relatively well-preserved organic matter compared to the hopanoids in the hydrocarbon fraction.

An obvious finding is that the range of hopanoic acids are shifted towards higher carbon numbers relative to the hopanes. While hopanes span from $C_{27}$ to $C_{31}$ in the hydrocarbon fractions, hopanoic acids range from $C_{30}$ to $C_{34}$. Farrimond et al. (2002) use the hopane carbon number distributions of different samples as an indicator for whether they have the same or different sources. The spread in carbon number distribution accompanied by the different isomerization indicate that hopanes and hopanoic acids of the calcite concretions do not have the same origin. Hopanes with the exception of hop-17(21)-ene seem to be considerably older and to have a terrestrial origin, similar to the long-chain *n*-alkanes, whereas hopanoic acids more likely came from the water column or from unknown sedimentary bacteria.

Hop-17(21)-ene is, in contrast to the other hopanes, an early degradation product and its abundance increases after decalcification. Although various hopanes and hopanoic acids are more abundant in the fractions after decalcification than before, the occurrence of hop-17(21)-ene is of greater significance, as it can be better related to its biological precursor than the others. The fact that unsaturated fatty acids are seen as too unstable to be primary here, while the unsaturated hopanoid is not, can be explained with the greater stability of the double bond, lying within the protecting, rather resistant hopanoid hydrocarbon skeleton (pers. comm. D. Birgel). Accordingly, with hop-17(21)-ene, the hydrocarbon fraction bears indeed a rather specific, significant indicator for bacteria involved in concretion formation. The occurrence of short-chain, branched fatty acids, together with hop-17(21)-ene, the depletion of $^{13}$C and the observation of framboidal pyrite in the thin sections imply the former presence of sulfate-reducing bacteria within the calcite concretions.

Similar assumptions cannot be made for siderite concretions, at least not solely based on their biomarker inventory. Biomarkers of the siderite concretion are sparse, unspecific and especially the decalcified fraction is almost barren of any lipids. GAMS4_12 entirely lack hopanoic acids, hopanes disappear after decalcification and branched fatty acids are less abundant after decalcification. As a consequence, it must be concluded that the molecular fossils are not intrinsic to the carbonate matrix; they mainly consist of allochthonous contribution of fatty acids from the water column. The only signal, which seems to be carbonate-bound, are long-chain *n*-alkanes and very unspecific *n*-fatty acids, but the relative content of aquatic material is overall higher compared to the calcite concretions (compare TAR and LMW/HMW). This pattern most probably reflects the higher age and degree of alteration and the marine origin of the siderite concretions. Statements about bacterial or archaean activity cannot be made based on biomarkers only. However, carbon and oxygen isotopes are typical for bacterial organic matter degradation and hence, bacterial iron reduction, a possible explanation, which is supported by the particular mineralogical composition of the concretions.

# 6 Conclusions

## 6.1 Calcite concretions

Calcite concretions formed around 10 Ma ago, in the southern Vienna Basin, a setting, which was first fully marine and part of the central Paratethys. The area was separated from the Paratethys and experienced significant inflow of freshwater, which subsequently led to the development of the brackish to limnic Pannonian Lake. A part of the Pannonian Lake, the later sandpit of Steinbrunn, was situated nearby the elevated area of the Leithagebirge from which it received reworked limestone with abundant corallinaceans from the prior, marine stage. The limestone was deposited together with siliciclastics and terrestrial plant detritus by fluvial transport from the adjacent continent. Earlier on the material was more fine-grained and contained more organic matter than the later deposits, which had a higher portion of carbonate, representing an increasingly shallower sedimentation realm, most likely a flood plain (Grundtner et al., 2009). During continued deposition, the buried fine-grained deposits experienced diagenesis, including oxidation of its organic matter. The organic matter was abundant enough that oxygen in the sediment was consumed entirely, and with continuing burial the conditions became anoxic. Although the environment was not fully marine any more, the pore water still contained sufficient sulfate to enable further oxidation of organic matter by bacterial sulfate reduction. Organic carbon was oxidized to bicarbonate and sulfate was reduced to sulfide. The reaction enhanced carbonate alkalinity and lowered the pH. The latter effect counteracted by precipitation of iron sulfides, which relied on reduction of ferric to ferrous iron, causing a net increase of pH. Carbonate supersaturation was reached and as the formation of framboidal pyrite consumed all the iron, an iron-free calcite microspar was precipitated in the pore space of the sediment. This happened in confined areas only, controlled by the localized activity of sulfate-reducing bacteria. Defined bodies of siliciclastic sediment were cemented by authigenic calcite and calcite concretions formed. The lipid biomarkers of the plant detritus and the sulfate-reducing bacteria were partly preserved in the calcite crystals. Also, stable carbon isotopes confirm that the carbonate is partly of organic matter origin. The other part very likely comprises detrital, marine limestone. The depletion of heavy oxygen isotopes of the concretions and their host sediment indicate a later influx of high-temperature and/or meteoric waters. The final volume of the concretions was probably already reached, while the interior was still in a sufficiently plastic state to allow the formation of septarian cracks (pervasive growth). The cracking could have been triggered by tectonic activity or by an excess pore pressure within the concretions due to loss of permeability by cementation.

## 6.2 Siderite concretions

With an age of 55 Ma the siderite concretions are considerably older than the calcite concretions of Steinbrunn and are products of an environment, which was very different from the geological background of the calcite concretions.

After the Northern Calcareous Alps were folded and thrusted during the orogenesis in the Early Cretaceous, they were continuously inundated by the Gosau sea from the north. The sediments, first terrestrial to shallow water, then deep water sediments, were deposited unconformably in the troughs and basins of the young orogen (Faupl, 2003). The basin of Gams repeatedly received turbidity currents, which formed massive layers of flysch, composed of sandy to silty successions and marl layers (Wagreich et al., 2011). The sedimentation rates were rather high, which caused depletion of seawater sulfate relative to the clastic material. Rapid burial led to the preservation of ferric iron in depth and as organic matter was also part of the turbidite layers, bacteria started to degrade it by ferric iron reduction. During alteration, the siderite concretions lost the molecular fossils of the iron-reducing bacteria, remaining organics do not seem to have been involved in their formation. Nevertheless, the isotopic signals of the concretions reveal the precipitation of organic-matter derived carbonate within marine pore waters. The rates of sulfate reduction were low enough to prevent the diffusion of hydrogen sulfide to the site of iron reduction. Both processes, sulfate reduction and iron reduction generated bicarbonate, but in contrast to sulfate reduction, iron reduction directly increases the pH. Partly in layers, partly patchy, conditions were reached, where iron reduction exceeded sulfate reduction and the concentration of hydrogen sulfide was too low to consume all the ferrous iron available. As a result, there was iron left to get incorporated into the carbonate minerals. Thin sections allow the assumption that first, when the iron concentration was very high, siderite microspar precipitated in the pores of the more fine-grained portions of the sediment. It seems that concretions did not form hard, dense layers before it reached its final dimensions, because bioturbation has been preserved. Then, a second iron-bearing carbonate formed, but the iron concentration was already too low for siderite, consequently, ferroan calcite filled the residual pore volume and completed the lithification of the siderite concretions and layers.

# 7 Acknowledgments

# 8 References

Antler G., Turchyn A.V., Rennie V., Herut B., Sivan O. (2013) Coupled sulfur and oxygen isotope insight into bacterial sulfate reduction in the natural environment. *Geochimica et Cosmochimica*, vol. 118, pp. 98–117.

Arning E.T., Birgel D., Brunner B., Peckmann J. (2009) Bacterial formation of phosphatic laminites off Peru. *Geobiology*, vol. 7, pp. 295–307.

Astin T.R. (1986) Septarian crack formation in carbonate concretions from shales and mudstones. *Clay Minerals*, vol. 21, pp. 617–631.

Birgel D., Thiel V., Hinrichs K.-U., Elvert M., Campbell, K.A., Reitner J., Farmer J.D., Peckmann J. (2006) Lipid biomarker patterns of methane-seep microbialites from the Mesozoic convergent margin of California. *Organic Geochemistry*, vol. 37, pp. 1289–1302.

Birgel D., Feng D., Roberts H.H., Peckmann J. (2011) Changing redox conditions at cold seeps as revealed by authigenic carbonates from Alaminos Canyon, northern Gulf of Mexico. *Chemical Geology*, vol. 285, pp. 82–96.

Birgel D., Meister P., Lundberg R., Horath T.D., Bontognali T.R.R., Bahniuk A.M., De Rezende C.E., Vasconcelos C., McKenzie J.A. (2015) Methanogenesis produces strong $^{13}$C enrichment in stromatolites of Lagoa Salgada, Brazil: a modern analogue for Palaeo-/Neoproterozoic stromatolites? *Geobiology*, vol. 13, pp. 245-266.

Bligh E.G., Dyer W.J. (1959) A rapid method of total lipid extractions and purification. *Canadian Journal of Biochemistry and Physiology*, vol. 37, pp. 911–917.

Blome C.D., Albert N.R. (1985) Carbonate concretions: An ideal sedimentary host for microfossils. *Geology*, vol. 13, pp. 212–215.

Blumenberg M., Krüger M., Nauhaus K., Talbot H.M., Oppermann B.I., Seifert R., Pape T., Michaelis W. (2006) Biosynthesis of hopanoids by sulfate-reducing bacteria (genus *Desulfovibrio*). *Environmental Microbiology*, vol. 8, pp. 1220–1227.

Bourbonniere R.A., Meyers P.A. (1996) Sedimentary geolipid records of historical changes in the watersheds and productivities of Lakes Ontario and Erie. *Limnology and Oceanography*, vol. 41, pp. 352–359.

Brocks J.J., Love G.D., Summons R.E., Knoll, A.H., Logan G.A., Bowden S.A. (2005) Biomarker evidence for green and purple sulphur bacteria in a stratified Palaeoproterozoic sea. *Nature*, vol. 437, pp. 866–870.

Coleman M.L. (1985) Geochemistry of diagenetic non-silicate minerals: kinetic considerations. *Philosophical Transactions of the Royal Society of London A*, vol. 315, pp. 39–56.

Coleman M.L., Hedrick D.B., Lovley D.R., White D.C., Pye K. (1993) Reduction of Fe(III) in sediments by sulphate-reducing bacteria. *Letters to Nature*, vol. 361, pp. 436–438.

Coleman M.L., Raiswell R. (1995) Source of carbonate and origin of zonation in pyritiferous carbonate concretions: evaluation of a dynamic model. *American Journal of Science*, vol. 295, pp. 282–308.

Dickson J.A.D (1965) A modified staining technique for carbonates in thin section. *Nature*, vol. 205, pp. 587-587.

Duan W.M., Hedrick D.B., Pye K., Coleman M.L., White D.C. (1996) A preliminary study of the geochemical and microbiological characteristics of modern sedimentary concretions. *Limnology and Oceanography*, vol. 41, pp. 1404–1414.

Duck R.W. (1995): Subaqueous shrinkage cracks and early sediment fabrics preserved in Pleistocene calcareous concretions. *Journal of the Geological Society, London*, vol. 152, pp. 151–156.

Eglinton G., Gonzalez A.G., Hamilton R.J., Raphael R.A. (1962). Hydrocarbon constituents of the wax coatings of plant leaves: a taxonomic survey. *Phytochemistry*, vol. 1, pp. 89–102.

Eickhoff M., Birgel D., Talbot H.M., Peckmann J., Kappler A. (2013) Bacteriohopanoid inventory of *Geobacter sulfurreducens* and *Geobacter metallireducens*. *Organic Geochemistry*, vol. 58, pp. 107–114.

El-Shafeiy M., Birgel D., El-Kammar A., El-Barkooky A., Wagreich M., Mohamed O., Peckmann J. (2014) Palaeoecological and post-depositional changes recorded in Campanian-Maastrichtian black shales, Abu Tartur plateau, Egypt. *Cretaceous Research*, vol. 50, pp. 38–51.

Elvert M., Boetius A., Knittel K., Jørgensen B.B. (2003) Characterization of specific membrane fatty acids as chemotaxonomic markers for sulfate-reducing bacteria involved in anaerobic oxidation of methane. *Geomicrobiology Journal*, vol. 20, pp. 403–419.

Farrimond P., Griffiths T., Evdokiadis E. (2002) Hopanoic acids in Mesozoic sedimentary rocks: their origin and relationship with hopanes. *Organic Geochemistry*, vol. 33, pp. 965–977.

Faupl P. (2003) *Historische Geologie*, 2nd ed., Facultas Verlags- und Buchhandels AG, Vienna, 271 p.

Gaines S.M., Eglinton G., Rullkötter J. (2009) *Echoes of life: what fossil molecules reveal about earth history*, Oxford University Press, Inc. New York, 355 p.

Gao X., Chen S., Xie X., Long A., Ma F. (2007) Non-aromatic hydrocarbons in surface sediments near the Pearl River estuary in the South China Sea. *Environmental Pollution*, vol. 148, pp. 40–47.

Grundtner M.-L. (2009) *Sedimentologisches Profil der Sandgrube Steinbrunn/Bgld.*, unpublished (Bachelorthesis), pp. 1–54.

Grundtner M.-L., Harzhauser M., Mandic O., Draganits E., Gier S., Exner U., Wagreich M. (2009) Zur Sedimentologie der Sandgrube Steinbrunn (Pannonium, Österreich). *Jahrbuch der Geologischen Bundesanstalt,* vol. 149, no. 4, pp. 441–451.

Guido A., Heindel K., Birgel D., Rosso A., Mastandrea A., Sanfilippo R., Russo F., Peckmann J. (2013) Pendant bioconstructions cemented by microbial carbonate in submerged marine caves (Holocene, SE Sicily). *Palaeogeography, Palaeoclimatology, Palaeoecology*, vol. 388, pp. 166–180.

Heindel K., Birgel D., Brunner B., Thiel V., Westphal H., Gischler E., Ziegenbalg S.B., Cabioch G., Sjövall P., Peckmann J. (2012) Post-glacial microbialite formation in coral reefs of the Pacific, Atlantic, and Indian Oceans. *Chemical Geology*, vol. 304-305, pp. 117–130.

Hoffmann-Sell L., Birgel D., Arning E.T., Föllmi K.B., Peckmann J. (2011) Archaeal lipids in Neogene dolomites (Monterey and Sisquoc Formations, California) – Planktic versus benthic archaeal sources. *Organic Geochemistry*, vol. 42, pp. 593–604.

Hounslow M.W. (1997) Significance of localized pore pressures to the genesis of septarian concretions. *Sedimentology*, vol. 44, pp. 1133–1147.

Irwin H., Curtis C., Coleman M. (1977) Isotopic evidence for source of diagenetic carbonates formed during burial of organic-rich sediments. *Nature*, vol. 269, pp. 209–213.

Kiriakoulakis K., Marshall J.D., Wolff G.A. (2000) Biomarkers in a Lower Jurassic concretion from Dorset (UK*). Journal of the Geological Society, London*, vol. 157, pp. 207–220.

Knoll A.H., Canfield D.E., Konhauser K.O. (2012) *Fundamentals of Geobiology*. Blackwell Publishing Ltd, 443 p.

Küpper H. (1951) *Exkursion in das südliche Wiener Becken und Randgebiete.* unpublished (fieldtrip guide), pp. 1–8.

Loeblich A.R., Tappan H.N (1987) *Foraminiferal genera and their classification*. Van Nostrand Reinhold, New York, 1694 p.

Loyd S.J., Berelson W.M., Lyons T.W., Hammond D.E., Corsetti F.A. (2012a) Constraining pathways of microbial mediation for carbonate concretions of the Miocene Monterey Formation using carbonate-associated sulfate. *Geochimica et Cosmochimica Acta*, vol. 78, pp. 77–98.

Loyd S.J., Corsetti F.A., Eiler J.M., Tripati A.K. (2012b) Determining the diagenetic conditions of concretion formation: assessing temperatures and pore waters using clumped isotopes. *Journal of Sedimentary Research*, vol. 82, pp. 1006–1016.

Loyd S.J., Dickson J.A.D., Boles J.R., Tripati A.K. (2014) Clumped-isotope constraints on cement paragenesis in septarian concretions. *Journal of Sedimentary Research*, vol. 84, pp. 1170–1184.

Mortimer R.J.G., Coleman M.L. (1997) Microbial influence on the oxygen isotopic composition of diagenetic siderite. *Geochimica et Cosmochimica Acta*, vol. 61, pp. 1705–1711.

Mortimer R.J.G., Galsworthy A.M.J., Bottrell S.H., Wilmot L.E., Newton R.J. (2011) Experimental evidence for rapid biotic and abiotic reduction of Fe(III) at low temperatures in salt marsh sediments: a possible mechanism for formation of modern sedimentary siderite concretions. *Sedimentology*, vol. 58, pp. 1514–1529.

Mozley P.S. (1989) Relation between depositional environment and the elemental composition of early diagenetic siderite. *Geology*, vol. 17, pp. 704–706.

Mozley P.S., Wersin P. (1992) Isotopic composition of siderite as an indicator of depositional environment. *Geology*, vol. 20, pp. 817–820.

Mozley P.S. (1996) The internal structure of carbonate concretions in mudrocks: a critical evaluation of the conventional concentric model of concretion growth. *Sedimentary Geology*, vol. 103, pp. 85–91.

Müller G., Gastner M. (1971) The "Karbonat-Bombe", a simple device for the determination of the carbonate content in sediments, soils and other materials. *Neues Jahrbuch für Mineralogie − Monatshefte*, vol. 10, pp. 466–469.

Pearson M.J., Hendry J.P., Taylor C.W., Russell M.A. (2005) Fatty acid in sparry calcite fracture fills and microsparite cement of septarian diagenetic concretions. *Geochimica et Cosmochimica Acta*, vol. 69, pp. 1773–1786.

Pearson M.J., Nelson C.S. (2005) Organic geochemistry and stable isotope composition of New Zealand carbonate concretions and calcite fracture fills. *New Zealand Journal of Geology & Geophysics*, vol. 48, pp. 395–414.

Peckmann J., Paul J., Thiel V. (1999) Bacterially mediated formation of diagenetic aragonite and native sulfur in Zechstein carbonates (Upper Permian, Central Germany). *Sedimentary Geology*, vol. 126, pp. 205–222.

Piller W.E., Decker K., Haas M. (1996) Exkursion A1: Sedimentologie und Beckendynamik des Wiener Beckens. Exkursionsführer SEDIMENT '96, *11. Sedimentologentreffen, Wien. – Berichte Geol. B.-A.*, vol. 33, pp. 41.

Pratt B.R. (2001) Septarian concretions: internal cracking caused by synsedimentary earthquakes. *Sedimentology*, vol. 48, pp. 189–213.

Pye K., Dickson J.A.D., Schiavon N., Coleman M.L., Cox M. (1990) Formation of siderite-Mg-calcite-iron sulphide concretions in intertidal marsh and sandflat sediments, north Norfolk, England. *Sedimentology*, vol. 37, pp. 325–343.

Raiswell R., Fisher Q.J. (2000) Mudrock-hosted carbonate concretions: a review of growth mechanisms and their influence on chemical and isotopic compostition. *Journal of the Geological Society, London*, vol. 157, pp. 239–251.

Raiswell R., Fisher Q.J. (2004) Rates of carbonate cementation associated with sulphate reduction in DSDP/ODP sediments: implications for the formation of concretions. *Chemical Geology*, vol. 211, pp. 71–85.

Reitner J., Peckmann J., Blumenberg M., Michaelis W., Reimer A., Thiel V. (2005) Concretionary methane-seep carbonates and associated microbial communities in Black Sea sediments. *Palaeogeography, Palaeoclimatology, Palaeoecology*, vol. 227, pp. 18–30.

Rohmer M., Bouvier-Nave P., Ourisson G. (1984) Distribution of hopanoid triterpenes in prokaryotes. *Journal of General Microbiology*, vol. 130, pp. 1137-1150.

Rommerskirchen F., Plader A., Eglinton G., Chikaraishi Y., Rullkötter J. (2006) Chemotaxonomic significance of distribution and stable carbon isotopic composition of long-chain alkanes and alkan-1-ols in C4 grass waxes. *Organic Geochemistry*, vol. 37, pp. 1303–1332.

Rontani J.-F., Bonin P. (2011) Production of pristane and phytane in the marine environment: role of prokaryotes. *Research in Microbiology*, vol. 162, pp. 923–933.

Rupp C. (1986) Paläoökologie der Foraminiferen in der Sandschalerzone (Badenien, Miozän) des Wiener Beckens. *Beiträge zur Paläontologie von Österreich*, vol. 12, pp. 1–180.

Rütters H., Sass H., Cypionka H., Rullkötter J. (2001) Monoalkylether phospholipids in the sulfate-reducing bacteria *Desulfosarcina variabilis* and *Desulforhabdus amnigenus*. *Archives of Microbiology*, vol. 176, pp. 435–442.

Sellés-Martínez J. (1996) Concretion morphology, classification and genesis. *Earth-Science Reviews*, vol. 41, pp. 177–210.

Siegel D.I, Chamberlain S.C., Dossert W.P. (1987) The isotopic and chemical evolution of mineralization in septarian concretions: Evidence for episodic paleohydrogeologic methanogenesis. *Geological Society of America Bulletin*, vol. 99, pp. 385–394.

Talbot H.M., Farrimond P.(2007) Bacterial populations recorded in diverse sedimentary biohopanoid distributions, *Organic Geochemistry*, vol. 38, pp. 1212–1225.

Thiel V., Blumenberg M., Kiel S., Leefman T., Liebenau K., Lindgren J., Sjövall P., Treude T., Zilla T. (2014) Occurrence and fate of fatty acyl biomarkers in an ancient whale bone (Oligocene, El Cien Formation, Mexico). *Organic Geochemistry*, vol. 68, pp. 71–81.

Thomka J.R., Lewis R.D. (2013) Siderite concretions in the Copan Crinoid Lagerstätte (Upper Pennsylvanian, Oklahoma): Implications for interpreting taphonomic and depositional processes in mudstone successions. *Palaios*, vol. 28, pp. 697–709.

Wagreich M., Egger H., Gebhardt H., Mohammed O., Spötl C., Koukal V., Hobiger G. (2011) A new expanded record of the Paleocene-Eocene transition in the Gosau Group of Gams (Eastern Alps, Austria). *Annalen des Naturhistorischen Museums in Wien*, vol. 113, pp. 35–65.

Wang L., Lee F.S.C., Wang X., Yin Y., Li J. (2007) Chemical characteristics and source implications of petroleum hydrocarbon contaminants in the sediments near major drainage outfalls along the coastal of Laizhou Bay, Bohai Sea, China. *Environmental Monitoring and Assessment*, vol. 125, pp. 229–237.

Wieninger A. (2009) Kalk-Konkretionen aus der Sandgrube Steinbrunn/Bgld., unpublished (Bachelorthesis), pp. 1–32.

Wilkin R.T., Barnes H.L. (1997) Formation processes of framboidal pyrite. *Geochimica et Cosmochimica Acta*, vol. 61, pp. 323-339.

Yli-Hemminki P., Jørgensen K.S., Lehtoranta J. (2014) Iron-manganese concretions sustaining microbial life in the Baltic Sea: The structure of the bacterial community and enrichments in metal-oxidizing conditions. *Geomicrobiology Journal*, vol. 31, pp. 263–275.

Zheng Y.-F. (1999) Oxygen isotope fractionation in carbonate and sulfate minerals. *Geochemical Journal*, vol. 33, pp. 109–126.

Ziegenbalg S.B., Brunner B., Rouchy J.M., Birgel D., Pierre C., Böttcher M.E., Caruso A., Immenhauser A., Peckmann J. (2010) Formation of secondary carbonates and native sulphur in sulphate-rich Messinian strata, Sicily. *Sedimentary Geology*, vol. 227, pp. 37–50.

Ziegenbalg S.B., Birgel D., Hoffmann-Sell L., Pierre C., Rouchy J.M., Peckmann J. (2012) Anaerobic oxidation of methane in hypersaline Messinian environments revealed by ^{13}C-depleted molecular fossils. *Chemical Geology*, vol. 292-293, pp. 140–148.

# 9 Appendix

**Nomenclature of Hopanoids**

| Trivial name | IUPAC name | Formula | MWt | Possible precursor | underivatized hopanoic acids Formula | MWt |
|---|---|---|---|---|---|---|
| Trisnorhopene | 22,29,30-Trisnorhop-17(21)-ene | $C_{27}H_{44}$ | 368 | all hopanes | | |
| $\beta\beta$ Trisnorhopane | 17$\beta$(H)-22,29,30-Trisnorhopane | $C_{27}H_{46}$ | 370 | all hopanes | | |
| $\alpha\beta$ Norhopane | 17$\alpha$(H),21$\beta$(H)-30-Norhopane | $C_{29}H_{50}$ | 398 | all hopanes | | |
| no trivial name | Hop-17(21)-ene | $C_{30}H_{50}$ | 410 | diploptene | | |
| $\beta\alpha$ Normoretane | 17$\beta$(H),21$\alpha$(H)-30-Normoretane | $C_{29}H_{50}$ | 398 | all hopanes | | |
| $\alpha\beta$ Hopane | 17$\alpha$(H),21$\beta$(H)-Hopane | $C_{30}H_{52}$ | 412 | diplopterol or BHP | | |
| $\beta\beta$ Norhopane | 17$\beta$(H),21$\beta$(H)-30-Norhopane | $C_{29}H_{50}$ | 398 | all hopanes | | |
| $\alpha\beta$ Homohopane | 17$\alpha$(H),21$\beta$(H)-Homohopane | $C_{31}H_{54}$ | 426 | BHP | | |
| $\beta\alpha$ Homomoretane | 17$\beta$(H),21$\alpha$(H)-Homomoretane | $C_{31}H_{54}$ | 426 | BHP | | |
| $\beta\beta$ Hopane | 17$\beta$(H),21$\beta$(H)-Hopane | $C_{30}H_{52}$ | 412 | diplopterol or BHP | | |
| $\beta\beta$ Homohopane | 17$\beta$(H),21$\beta$(H)-Homohopane | $C_{31}H_{54}$ | 426 | BHP | | |
| $\alpha\beta$ Hopenoic acid | 17$\alpha$(H),21$\beta$(H)-Hopenoic acid ME | $C_{31}H_{50}O_2$ | 454 | diploptene | $C_{30}H_{49}O_2$ | 440 |
| $\alpha\beta$ Hopanoic acid | 17$\alpha$(H),21$\beta$(H)-Hopanoic acid ME | $C_{31}H_{52}O_2$ | 456 | diplopterol or BHP | $C_{30}H_{50}O_2$ | 442 |
| $\beta\beta$ Homohopenoic acid | 17$\beta$(H),21$\beta$(H)-Homohopenoic acid ME | $C_{32}H_{52}O_2$ | 468 | BHP | $C_{31}H_{51}O_2$ | 455 |
| $\beta\alpha$ Hopanoic acid | 17$\beta$(H),21$\alpha$(H)-Hopanonic acid ME | $C_{31}H_{52}O_2$ | 456 | diplopterol or BHP | $C_{30}H_{50}O_2$ | 442 |
| $\alpha\beta$ Homohopanoic acid | 17$\alpha$(H),21$\beta$(H)-Homohopanoic acid ME | $C_{32}H_{54}O_2$ | 470 | BHP | $C_{31}H_{52}O_2$ | 456 |
| $\beta\beta$ Hopanoic acid | 17$\beta$(H),21$\beta$(H)-Hopanoic acid ME | $C_{31}H_{52}O_2$ | 456 | diplopterol or BHP | $C_{30}H_{50}O_2$ | 442 |
| $\beta\alpha$ Homohopanoic acid | 17$\beta$(H),21$\alpha$(H)-Homohopanoic acid ME | $C_{32}H_{54}O_2$ | 470 | BHP | $C_{31}H_{52}O_2$ | 456 |
| $\beta\beta$ Bishomohopenoic acid | 17$\beta$(H),21$\beta$(H)-Bishomohopenoic acid ME | $C_{33}H_{54}O_2$ | 482 | BHP | $C_{32}H_{53}O_2$ | 469 |
| $\alpha\beta$ Bishomohopanoic acid | 17$\alpha$(H),21$\beta$(H)-Bishomohopanoic acid ME | $C_{33}H_{56}O_2$ | 484 | BHP | $C_{32}H_{54}O_2$ | 470 |
| $\beta\beta$ Homohopanoic acid | 17$\beta$(H),21$\beta$(H)-Homohopanoic acid ME | $C_{32}H_{54}O_2$ | 470 | BHP | $C_{31}H_{52}O_2$ | 456 |
| $\beta\beta$ Bishomohopanoic acid | 17$\beta$(H),21$\beta$(H)-Bishomohopanoic acid ME | $C_{33}H_{56}O_2$ | 484 | BHP | $C_{32}H_{54}O_2$ | 470 |
| $\alpha\beta$ Trishomohopanoic acid | 17$\alpha$(H),21$\beta$(H)-Trishomohopanoic acid ME | $C_{34}H_{58}O_2$ | 498 | BHP | $C_{33}H_{56}O_2$ | 484 |
| $\beta\beta$ Trishomohopanoic acid | 17$\beta$(H),21$\beta$(H)-Trishomohopanoic acid ME | $C_{34}H_{58}O_2$ | 498 | BHP | $C_{33}H_{56}O_2$ | 484 |
| $\beta\beta$ Tetrakishomohopanoic acid | 17$\beta$(H),21$\beta$(H)-Tetrakishomohopanoic acid ME | $C_{35}H_{60}O_2$ | 512 | BHP | $C_{34}H_{58}O_2$ | 498 |

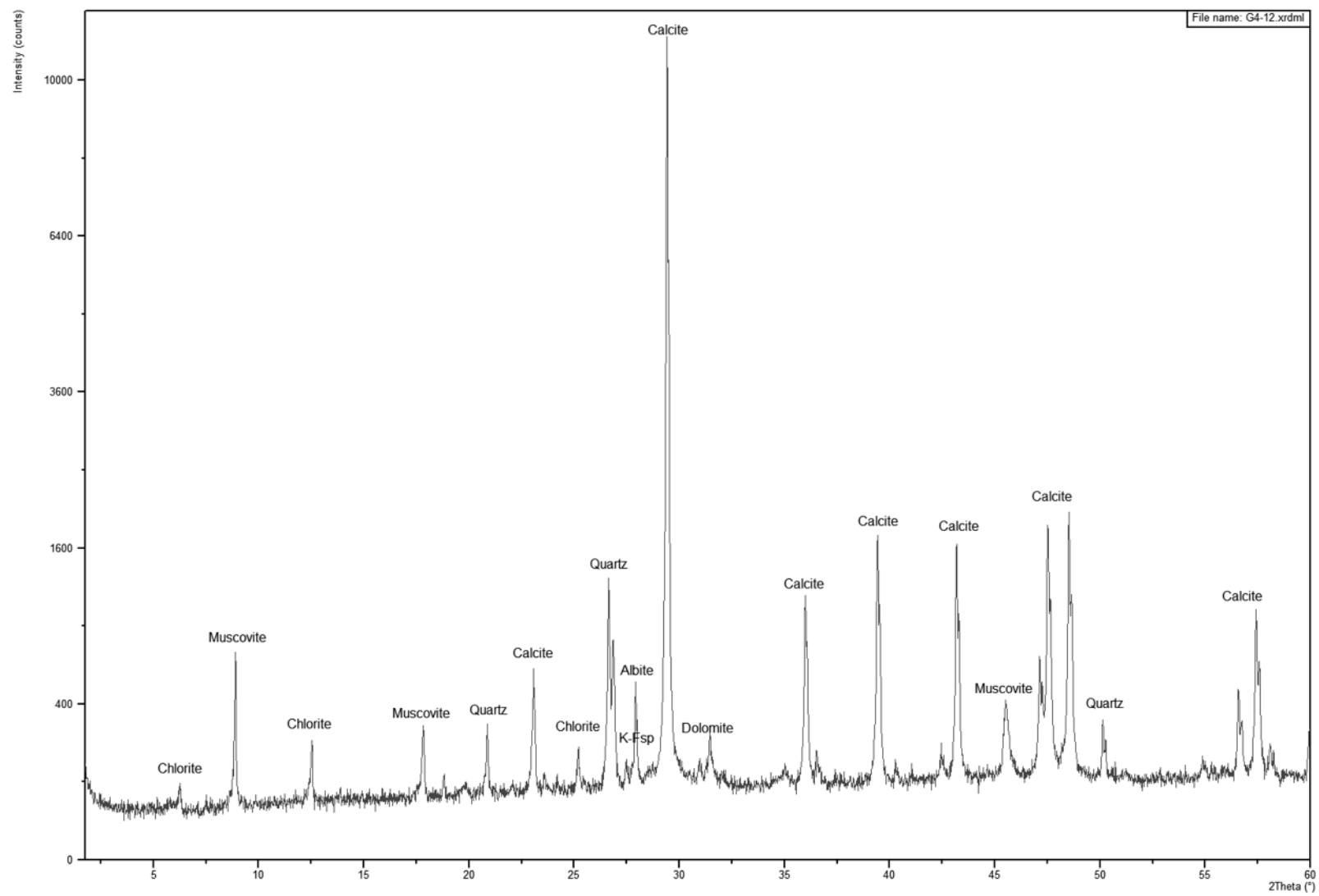Table I: Nomenclature of hopanes and hopanoic acids. MWt = molecular weight; BHP = bacteriohopanepolyols; ME = methyl.

Table II: Powder X-ray diffractogram of calcite concretion G4_12.

# Curriculum vitae

**<u>Education:</u>**

| | |
|---|---|
| Since 2013 | MSc-study Earth Sciences (core area in geology at the University of Oviedo (Spain) and the University of Vienna (date of expected award: July 2015) |
| 2009 -2013 | BSc-study Earth Sciences at the University of Vienna |
| 2004 - 2009 | Commercial college: Bundeshandelsakademie Amstetten (Austria), graduation with "excellent success" |
| 2000 - 2004 | Secondary school: Hauptschule Euratsfeld (Austria) |
| 1996 - 2000 | Primary school: Volksschule Ferschnitz (Austria) |

**<u>Work experiences:</u>**

| | |
|---|---|
| September 2014 | Analysis of pearls' surfaces with SEM (Natural History Museum of Vienna) |
| June 2014 | Tutorship at an actuo-paleontology fieldtrip in Friuli/Italy (University of Vienna) |
| June 2014 | Tutorship at the fieldtrip "field mapping" in Carinthia/Austria (University of Vienna) |
| March-June 2014 | Tutorship in sedimentology (University of Vienna) |
| November 2013 | Fair promotion (Border Concepts) |
| August 2013 | Fundraising (AIWWF) |
| July 2013 | Paleoseismological Trench (Project of OMV, carried out by the University of Vienna) |
| October – January 2012 | Tutorship in geological history and stratigraphy (University of Vienna) |
| October – January 2011 | Tutorship in geological history and stratigraphy (University of Vienna) |
| September 2010 | Post-delivery (Post AG) |
| August 2008 | Unskilled labour (Municipality of Wang) |

**<u>Personal skills:</u>**

| | |
|---|---|
| Mother tongue: | German |
| Other languages: | English (fluent) |
| | Spanish (fluent) |
| | Russian (Cyrillic script and basic knowledge) |
| | |
| Driving licence: | European driving licence class B |

| | |
|---|---|
| Computer skills: | European Computer Driving Licence (ECDL, at commercial college) |
| | ArcMAP from ArcGIS |
| | Petrel |
| | |
| Analytical skills: | Extraction and analysis of lipid biomarkers from sediment samples measured on GC-FID, GC-MS |
| | Dissolution-precipitation experiments on fish vertebrae |
| | Infrared (IR) spectroscopy |
| | Course about scanning electron microscopy (SEM) |
| | Identification of opaque minerals with reflected-light microscopy |
| | Identification of transparent minerals with polarisation microscopy |
| | Production of thin sections |
| | Sample preparation for X-ray luminescence (XRL) analysis |
| | (For further explanations see "Techniques and methods used in the past") |

**<u>Research interests</u>**

Geobiology
Chemical and biochemical sedimentary rocks
Sedimentary geochemistry and element cycles
Sedimentogenic ore deposits
Fluid fluxes in surface and subsurface systems
Redoxindicators, especially of the Precambrian
Early life